Topographic and geologic controls of frost cracking in Alpine rockwalls

Daniel Draebing[1] and Till Mayer[1]

[1]University of Bayreuth

November 26, 2022

Abstract

Frost weathering is a major control of rockwall erosion in alpine environments. Previous frost cracking model approaches used air temperatures as a proxy for rock temperatures to drive frost weathering simulations on rockwall and on mountain scale. Unfortunately, the thermal rockwall regime differs from air temperature due to topographic effects on insolation and insulation, which affects frost weathering model results and the resulting erosion patterns. To provide a more realistic model of the rockwall regime, we installed six temperature loggers along an altitudinal gradient in the Swiss Alps including two logger pairs at rockwalls with opposing aspects. We used the recorded rock surface temperatures to model rock temperatures in the upper 10 m of the rockwalls and as input data to run four different frost cracking models. We mapped fracture spacing and rock strength to validate the model results. Our results showed that frost cracking models are sensitive to thermal, hydraulic and mechanical parameters that affect frost cracking magnitude, while frost cracking patterns in terms of peak location and affected rock mass were consistent. Thermo-mechanical models incorporate rock strength and hydraulic properties and provided a frost cracking depth pattern at rockwall scale that reflects better measured rock strength and fracture spacing of the simulated rock masses. On mountain scale, these models showed a pattern of increasing frost cracking with altitude, which is contrary to purely thermal models but consistent with observations of existing rockfall studies.

Topographic and geologic controls of frost cracking in Alpine rockwalls

D. Draebing[1,2,3] and T. Mayer[1,3]

[1]Chair of Geomorphology, University of Bayreuth, Germany.

[2]Department of Physical Geography, Utrecht University, Utrecht, Netherlands.

[3]Chair of Landslide Research, Technical University of Munich, Germany.

Corresponding author: Daniel Draebing (d.draebing@uni-bayreuth.de)

Key Points:

- Temperature loggers provide rock temperature data that incorporates topographic effects on insolation and insulation.
- Sensitivity tests on frost cracking models showed differences of frost magnitude while frost cracking depth patterns were consistent.
- Thermo-mechanical models incorporating rock strength and hydraulic properties produced more realistic altitudinal frost cracking patterns.

Abstract

Frost weathering is a major control of rockwall erosion in alpine environments. Previous frost cracking model approaches used air temperatures as a proxy for rock temperatures to drive frost weathering simulations on rockwall and on mountain scale. Unfortunately, the thermal rockwall regime differs from air temperature due to topographic effects on insolation and insulation, which affects frost weathering model results and the resulting erosion patterns. To provide a more realistic model of the rockwall regime, we installed six temperature loggers along an altitudinal gradient in the Swiss Alps including two logger pairs at rockwalls with opposing aspects. We used the recorded rock surface temperatures to model rock temperatures in the upper 10 m of the rockwalls and as input data to run four different frost cracking models. We mapped fracture spacing and rock strength to validate the model results. Our results showed that frost cracking models are sensitive to thermal, hydraulic and mechanical parameters that affect frost cracking magnitude, while frost cracking patterns in terms of peak location and affected rock mass were consistent. Thermo-mechanical models incorporate rock strength and hydraulic properties and provided a frost cracking depth pattern at rockwall scale that reflects better measured rock strength and fracture spacing of the simulated rock masses. On mountain scale, these models showed a pattern of increasing frost cracking with altitude, which is contrary to purely thermal models but consistent with observations of existing rockfall studies.

Plain Language Summary

Frost weathering is an important mechanism of shaping rockwalls in alpine environments. Previous studies developed purely thermal and thermo-mechanical models incorporating mechanical and hydraulic parameters to simulate this process. Both model types provide valuable insights about a process that is hard to measure. Previous model approaches used air temperature as input data. Unfortunately, rock temperatures differ from air temperatures due to topography that changes the insolated surface of rockwalls and insulating snow cover. We measured rock temperatures directly at six rockwalls with different aspects and lithology along a large range of altitude. We used our data to run four existing frost weathering models. Our results show that the rock type, strength of rocks and water availability influences the magnitude of frost weathering, while frost cracking location and affected rockwall depth does not change. The frost cracking pattern should be reflected by the fracture network and the strength of rockwalls. We mapped fractures and measured rock strength and our results correspond better to thermo-mechanical model results. Thermo-mechanical model results show an increase of frost weathering with increasing altitude. This pattern is consistent with rockfall observations. In contrast, purely thermal models showed an inverse relationship with higher frost cracking at lower altitudes.

1 Introduction

The interplay of tectonic, climatic and erosion processes controls topography and in turn steep alpine environments are characterized by high erosion rates [*Montgomery & Brandon*, 2002; *Whipple et al.*, 1999]. Climate affects mechanical weathering including frost cracking processes [*Eppes & Keanini*, 2017] that breakdown rock [*Matsuoka & Murton*, 2008]. This rock is subsequently transported by rockfall processes [*Krautblatter & Dikau*, 2007] and results in erosion of rockwalls. Rockwall erosion depends also on in situ stress, geological, hydrological and biological conditions as well as time [*Krautblatter & Moore*, 2014]. Therefore, a spatial and temporal detection of rockfall using laserscanning and seismic monitoring cannot identify frost cracking, however, previous studies gave a likelihood of potential rock breakdown processes and highlighted the importance of frost weathering as preparing and triggering factor of rockfall [e.g. *Dietze et al.*, 2017; *Strunden et al.*, 2015].

Field measurements of rockwall erosion using rockfall collectors suggest that rockfall is influenced by seasonal ice segregation [*Matsuoka*, 2019; *Matsuoka & Sakai*, 1999; *Sass*, 2005c] and volumetric expansion caused by short-term freezing [*Fahey & Lefebure*, 1988; *Matsuoka*, 2019; *Sass*, 2005c], which both are controlled by moisture supply [*Rode et al.*, 2016; *Sass*, 2005a, 2005c]. If rockfall deposits are not reworked by glaciers [e.g. *Scherler et al.*, 2011] or rivers [e.g. *Schrott et al.*, 2003], long-term rockfall results in scree slope formation [*Statham*, 1976]. The spatial distribution of scree slopes suggest a climatic control by frost weathering on a regional scale [*Hales & Roering*, 2005; *Thapa et al.*, 2017]. Erosion rates derived from talus slopes [*Sass*, 2010] and spatially distributed rockfall collectors [*Sass*, 2005b] indicate an increase of rockfall supply from north-facing permafrost affected rockwalls on short-term (up to five years) and mid-term scale [aproximately 400 years; *Sass*, 2010]. On Holocene scale, talus slope deposits suggest an increased rockwall erosion rate at north-facing compared to south-facing rockwalls [*Sass*, 2007].

The efficacy of different frost weathering processes has been discussed since the 1980s [*McGreevy & Whalley*, 1985; *Walder & Hallet*, 1986]. Volumetric expansion by freezing ice occurs during short-term freezing cycles and can produce stresses as high as 207 MPa [*Matsuoka & Murton*, 2008]. Field measurements suggest that these processes occur during freezing periods in late autumn and due to refreezing of meltwater in late spring and summer [*Matsuoka*, 2001, 2008]. In contrast, ice segregation occurs during sustained freezing conditions due to cryosuction-induced stresses [*Matsuoka & Murton*, 2008]. Laboratory [*Duca et al.*, 2014; *Hallet et al.*, 1991; *Murton et al.*, 2006] and field studies [*Draebing et al.*, 2017b; *Weber et al.*, 2018] support the importance of ice segregation for frost weathering. Recently, *Draebing and Krautblatter* [2019] tested the efficacy of volumetric expansion and ice segregation on fractured rock in geometrically defined cracks. Fractures in rock can grow when stresses exceed the strength properties of rock (critical cracking), however, cracks can also grow steadily at stresses below critical levels [subcritical cracking; *Eppes & Keanini*, 2017]. *Draebing and Krautblatter* [2019] quantified volumetric expansion of saturated fractures and demonstrated that resulting stresses exceeded strength properties of rocks. Therefore, volumetric expansion is highly effective but unlikely due to a lack of saturation of fractures in the field. In contrast, ice segregation on seasonal scale produced stresses in the subcritical range [*Draebing & Krautblatter*, 2019]. The ice-induced stresses started to occur at a temperature between -0.04°C and -2.35°C depending on lithology [*Draebing & Krautblatter*, 2019] at pore water availability ranges that are common in Alpine rockwalls [*Girard et al.*, 2013; *Sass*, 2005a]. Field measurements of frost cracking and ice-induced crack widening at or near the rock surface [*Amitrano et al.*, 2012; *Draebing et al.*, 2017b; *Girard et al.*, 2013] and in rock depth of 20 m [*Wegmann & Gudmundsson*, 1999; *Wegmann & Keusen*, 1998] demonstrated that frost cracking occurs at the full temperature range between 0 and -15° C. Sustained freezing results in higher frost cracking activity than frequent freeze-thaw cycling [*Amitrano et al.*, 2012; *Girard et al.*, 2013], however, field studies are unable to distinguish the roles of volumetric expansion and ice segregation in frost cracking.

Different frost cracking models have been developed to model ice segregation induced weathering. Thermo-meachnical models include lithological and hydrological effects [*Walder & Hallet*, 1985] and were successfully used to model frost cracking at laboratory [*Murton et al.*, 2006] and rockwall scale [*Sanders et al.*, 2012]. At geomorphic scales such as landscapes, it is difficult to relate the physics of ice growth to rock breakdown by frost cracking and rockwall erosion by rockfall. A simple empirical frost cracking model using elevation dependent air temperature was developed by *Hales and Roering* [2007] to model spatial and temporal patterns of rockwall erosion. This model was applied in studies in the European Alps [*Delunel et al.*, 2010; *Messenzehl et al.*, 2018; *Savi et al.*, 2015], New Zealand Alps [*Hales & Roering*, 2009], Himalayas [*Orr et al.*, 2019; *Scherler*, 2014] or Oregon Coast range [*Marshall et al.*, 2015; *Marshall et al.*, 2017]. Resulting frost cracking intensity was validated using fracture spacing as a proxy for rock mass susceptibility for frost weathering [*Hales & Roering*, 2007, 2009; *Messenzehl et al.*, 2018] or compared to erosion rates [*Delunel et al.*, 2010; *Marshall et al.*, 2015; *Marshall et al.*, 2017; *Savi et al.*, 2015]. *Anderson et al.* [2013] extended the model to simulate long-term development of periglacial landscapes. Recently *Rempel et al.* [2016] developed a thermo-mechanical model based on the model by *Walder and Hallet* [1985] to incorporate ice physics without losing the applicability at geomorphic scales. *Marshall et al.* [2021] applied the model in combination with climate simulations to model frost weathering in unglaciated North America during the Last Glacial Maximum. The different models use air temperature as a proxy for rock temperature [e.g. *Hales & Roering*, 2007; *Rempel et al.*, 2016], however, previous permafrost studies demonstrated that there is a significant temperature offset between air and rockwall temperatures [e.g. *Hasler et al.*, 2011b; *Magnin et al.*, 2015]. Furthermore, the models assume thermal, hydrologic and mechanical properties of rocks, however, previous studies have not tested yet how these properties influence model results at rockwall and mountain scales. For this purpose, we installed six rock temperature loggers along an altitudinal transect including different aspects and different lithology. We use obtained rock temperature data to (1) model frost cracking activity on rockwall scale applying the models by *Hales and Roering* [2007], *Anderson et al.* [2013], *Walder and Hallet* [1985] and *Rempel et al.* [2016]. We (2) test the sensitivity of these models for rock thermal diffusivity, hydraulic properties, initial crack length and fracture toughness. We (3) map fracture spacing and quantify rock strength in the field as a proxy for frost weathering and compare the data to frost cracking model results on rockwall and mountain scale.

2 Study site

Research was conducted in the Hungerli Valley and Steintaelli, Swiss Alps (Fig. 1a-b). The Hungerli Valley is an east to west oriented hanging valley of the Turtmann Valley (Fig. 1c), while the Steintaelli is a 50 m northeast (NE) to southwest (SW) orientated ridge on the crestline between Matter and Turtmann Valley (Fig. 1d). Lithology consists of paragneiss, manly schisty quartz slate with inclusions of aplite and quartzite in the Rothorn (RH) cirque (Fig. 1e) and amphibolite in the Hungerlihorli [HH, Fig. 1c; *Bearth*, 1980]. Rockwalls reach from 2400 m up to the Rothorn at 3277 m. Adjacent to the rockwalls, talus slopes formed by rockfall processes store one fifth of the sediment of the Hungerli Valley [*Otto et al.*, 2009]. In the Steintaelli, geophysical measurements indicated the occurrence of permafrost on the NE-facing slope, while permafrost was absent in the SW slope between 2006 and 2019 [*Draebing et al.*, 2017a; *Krautblatter & Draebing*, 2014; *Scandroglio et al.*, 2021]. Permafrost distribution is strongly controlled by snow cover, which resulted in 3.7 to 3.9 °C colder mean annual rock surface temperature (MARST) at the NE compared to SW slope [*Draebing et al.*, 2017a]. Snow cover influenced cryogenic and thermal processes that resulted in fracture opening due to ice segregation on the crest and thermal induced fracture dynamics on the SW slope [*Draebing et al.*, 2017b].

3 Methods

We conducted measurements at rockwalls ranging from 2580 to 3158 m to identify the influence of altitude on frost weathering (Fig. 2a). To determine the influence of aspect, we investigated two rockwalls (RW1 and RW3) at similar altitudes with opposing north and south expositions.

3.1 Rockwall and rock mechanical data

To validate the effect of frost cracking, we conducted horizontal and vertical scanline measurements [*Priest*, 1993] at RW2 to RW4 and re-analyzed previous conducted measurements at RW1 [*Halla*, 2013]. Based on these measurements, we calculated the fracture spacing [*Priest*, 1993], which will be compared to the depth and peaks of modelled frost cracking [*Hales & Roering*, 2007, 2009; *Messenzehl et al.*, 2018]. We quantified rock strength using Schmidt hammer measurements, which are a common tool to quantify effects of near surface weathering [*McCarroll*, 1991; *Murphy et al.*, 2016; *Shobe et al.*, 2017] including frost weathering [*Matsuoka*, 2008; *Matthews et al.*, 1986]. We compared measured rock strength to near surface model results of frost cracking. Furthermore, we evaluated rock mass strength using the method by *Selby* [1980]. We collected several 0.4 x 0.2 x 0.15 m large schisty quartz slate samples from the talus slope below RW4, amphibolite samples below RW3-N and aplite samples below RW2. We assume that talus slope samples represent mechanical properties of the adjacent rockwalls. We quantified rock sample anisotropy [*Draebing & Krautblatter*, 2012], Young modulus E, Poisson' ratio v, shear modulus G using seismic laboratory measurements (see Text S1 in the Supporting information). Rock porosity φ_r and density ρ_r were measured following the German industry norm (DIN 52102, DIN EN 1097-6). We derived uniaxial compressive strength σ_u [*Mutschler*, 2004], tensile strength σ_t [*Lepique*, 2008] and estimated fracture toughness K_C [*Chang et al.*, 2002; *Zhang*, 2002].

3.2 Meteorological and rock temperature data

We use air temperature (AT) and snow depth data obtained from Oberer Stelligletscher (2910 m), located on flat terrain 2-3 km southeast (SE) of our study area in the Matter Valley [*MeteoSwiss*, 2019b]. The data shows a gap from mid-January to end of February 2018 (Fig. 2a), probably as a result of intense snow depth (>3.5 m). To fill the gap, we adapted air temperature from near-by (6.5 km) meteo station Grächen [*MeteoSwiss*, 2019a], located at 1605 m in the

Matter Valley using a linear correlation (r^2= 0.85). The temperature adjustment corresponds to a lapse rate of 6 °C km^{-1}.

Rock surface temperatures depend on topography, snow cover, fracturing and water availability. Topography changes the insolated geometry and results in solar radiation differences [*Gruber et al.*, 2004; *Hasler et al.*, 2011b], while snow cover can build up from ledges and reach a thickness of several meters at rockwalls [*Haberkorn et al.*, 2017; *Phillips et al.*, 2017; *Wirz et al.*, 2011] insulates the rock surface [*Haberkorn et al.*, 2015a; *Haberkorn et al.*, 2015b]. Fracturing increases surface roughness and the ability to retain snow [*Gruber & Haeberli*, 2007], increases convective heat flow by air [*Moore et al.*, 2011] and advective heat flow by water [*Gruber & Haeberli*, 2007; *Hasler et al.*, 2011a; *Phillips et al.*, 2016] as well as water availability and permeability [*Dietrich et al.*, 2005; *Gruber & Haeberli*, 2007]. To monitor rock surface temperature (RST), we installed six Maxim iButton DS1922 L temperature loggers in 10 cm deep boreholes following the measurement method by previous studies [e.g. *Draebing et al.*, 2017a; *Haberkorn et al.*, 2015b]. Temperature loggers have a nominal accuracy of ±0.5 °C according to the manufacturer, however, zero curtain occurrence suggest an accuracy of ±0.25 °C at the freezing point. The loggers recorded RST in 3 h intervals between 1 September 2016 and 31 August 2019 (RW2, RW3-N, and RW4) or between 1 September 2017 and 31 August 2019 (RW1-N, RW1-S, and RW3-S), respectively. Snow cover and zero curtain duration can be detected in RST time series using daily standard deviations due to insulating properties of snow [*Haberkorn et al.*, 2015a; *Schmid et al.*, 2012]. We applied the uniform standard deviation threshold of <0.5 K for positive and negative RST by *Haberkorn et al.* [2015b], which was previously validated in a study in the Steintaelli [*Draebing et al.*, 2017a]. We calculated mean annual air temperature (MAAT) and adapted air temperature to logger elevations by using the temperature lapse rate. To compare temperature logger locations, we calculated the mean annual rock surface temperature (MARST). We calculated mean winter and mean summer air/rock surface temperatures to anaylse seasonal effects. We calculated a 10-day running average of air and rock surface temperatures and calculated the thermal offset that should reflect insolation and insulation effects.

To model rock temperatures up to 10 m depth in 0.1 m resolution steps, we use a 1D conductive heat model applying the Fourier Equation [*Carslaw & Jaeger*, 1986] and incorporate latent heat effects as previous studies [e.g. *Anderson et al.*, 2013; *Hipp et al.*, 2014]. Rock porosity of the rock samples are below 1 % (Table 2). In contrast to intact rock samples, rock masses of rockwalls consist of fractures. These fractures are incorporated into the model by increasing the rockwall porosity to 3 %. We assume that the pores and fractures are fully saturated. Therefore, we assume isotropic rocks as done in previous rock temperature model approaches [e.g. *Draebing et al.*, 2017a; *Noetzli & Gruber*, 2009; *Noetzli et al.*, 2007; *Wegmann et al.*, 1998; *Wegmann & Keusen*, 1998]. However, rock masses are anisotropic due to the existence of fractures and our model approach neglects advective heat transport by water flow and convective heat transport by wind along fractures. For details on the model-processing see Text S2 in the supporting information and for used parameters see Table 2.

3.3 Frost Cracking Modeling

To evaluate frost weathering in the different rockwalls, we used our rock temperature data to drive four different frost weathering model approaches. The purely thermal models by

Hales and Roering [2007; HR-Model] and *Anderson et al.* [2013; A-Model] assume that the frost cracking rate by ice segregation is proportional to the temperature gradient, therefore, they use the temperature gradient as a proxy for cracking intensity. Both model approaches assume that frost cracking will occur in a temperature range between -8 and -3 °C established as the frost cracking window (FCW) by *Anderson* [1998]. The second assumption is the water availability. In the model by *Hales and Roering* [2007], water is available, when rock surface temperatures are above 0 °C (upper boundary) and the temperature gradient is negative or rock temperatures in 10 m depths are above 0 °C (lower boundary) and the temperature gradient is positive. The model by *Anderson et al.* [2013] assumes water available at a rock temperature above 0 °C anywhere along the one-dimensional path inside the rock mass, however, the water transport is restricted by a penalty function that modifies the taken temperature gradients dependent on their distance to the next water reservoir. If the temperature and water assumptions are fulfilled, both models sum up the temperature gradients and use this cracking intensity as a proxy for frost cracking.

We use two thermo-mechanical models to simulate frost weathering at rockwalls. Both models assume that a rockwall consists of pores of different shapes and sizes including non-equant voids called cracks. In their model, *Walder and Hallet* [1985] assume cracks have a penny-shaped form with an initial crack radius x_i of 0.05 m, which corresponds to a crack length of 0.1 m, and a crack plane parallel to the rockwall (φ_p=0°). These cracks are spaced widely enough to enhance independent growth. All cracks grow in a mode I form along the plane of the crack purely by ice pressure. In our model approach, we assume the existence of an independent crack at every model increment step of 0.1 m rock depth (Fig. 2). The model further assumes that the pore space of unfrozen rock is fully saturated at all times. Segregation ice growth starts for temperatures below the freezing point in pores T_f =-1°C, but only if an unfrozen rock mass area with water is available (T>T_f). One dimensional water migration in the model is restrained by the thermal gradient and the grain/pore surface resistivity (Text S3 in the supporting information).When ice pressure rises in the ice lens, an elastic opening of the crack occurs and deforms the crack into an oblate ellipsoid. Crack length grows inelastic if one third of the critical fracture toughness (K_c) is reached. We used hydraulic and mechanical parameters suggested by *Walder and Hallet* [1985] except for Poisson ratio, shear modulus and critical fracture toughness, which we measured in the laboratory (Table 2). To enable an annual comparison of crack growth, we started the simulation with an initial crack length of 0.1 m for every year (1 September to 31 August) to ensure comparability between years (Fig. 5). We summed up the final crack length at each year and divided this length by the rock depth of our model to get a quantitative measure to compare frost cracking at different rockwalls.

The model by *Rempel et al.* [2016] assumes a porosity change to occur alongside frost weathering. The authors determine an upper temperature limit ΔT_c for ice segregation depending on fracture toughness and crack radius (see Text S4 in the supporting information) and a lower limit of ice segregation controlled by permeability dependent water availability. We use the values suggested by *Rempel et al.* [2016; Table 2], unfrozen permeability measured by *Krautblatter* [2009] and laboratory defined critical fracture toughness. *Rempel et al.* [2016] integrate porosity change over depth to get the total expansion Λ resulting from ice segregation.

3.4 Sensitivity of frost cracking models

All frost cracking models are sensitive to the temperature gradient. The temperature gradient results from the rock temperature modelling using the Fourier equation that propagated heat using rock thermal diffusivity κ (= $k/c\rho_r$), which depends on rock thermal conductivity k, rock specific heat capacity c and rock density ρ_r. All parameters show a variation on rock sample scale, which will increase on rockwall scale. Therefore, rock thermal diffusivity comprises a range of values and we used a mean value for frost cracking modelling. To test the sensitivity to heat conduction, we additionally modelled the frost cracking using minimum and maximum values of rock diffusivity (Table 2).

The thermo-mechanical models by *Walder and Hallet* [1985] and *Rempel et al.* [2016] are in addition sensitive to hydraulic parameters such as conductivity or permeability, initial crack length and fracture toughness. Hydraulic permeability values range over magnitudes such as 10^{-18} to 10^{-12} m² [*Rempel et al.*, 2016]. We use the nominal value 10^{-14} m² by *Rempel et al.* [2016] and the measured value 10^{-18} m² by *Krautblatter* [2009] for the sensitivity test of the R-Model. To test the sensitivity of the WH-model to hydraulic properties, we increased the applied hydraulic conductivity (5 x 10^{-14} m s^{-1}) by four orders of magnitude to include a similar variation as in the R-model. Crack length varies in rocks [*Maji & Murton*, 2020] and needs to be assumed, therefore, we conducted tests using a crack length of 0.01 and 0.1 m. Fracture toughness varies between rock types and comprises a wide range within each rock type [*Atkinson*, 1984]. For our model approach, we used a mean value of fracture toughness derived from an estimation based on uniaxial strength measurements [*Chang et al.*, 2002]. For the sensitivity tests, we used in addition a minimum and maximum value (Table 2). The minimum value was derived from the Schmidt hammer tests according to *ISRM* [1978]. We estimated the maximum value based on tensile strength measurement on rock samples [*Zhang*, 2002].

4 Results

4.1 Rockwall mechanical properties

We used the Schmidt hammer rebound value R as a proxy for rock strength. Observed mean rock strength was highest at RW3-N (64, Table 1), which consists of amphibolite. Rockwalls consisting of schisty quartz slate showed a variation of mean rock strength and ranged from 31 at RW3-S, 39 at RW4, 46 at RW1-N to 53 at RW1-S. RW2 that comprise aplite had a mean rock strength of 49. Mean fracture spacing showed large spatial variation within schisty quartz slate rock masses ranging from 0.32 m at RW3-S, 0.67 m at RW4, 0.85 m at RW1-N to 2.82 m at RW1-S (Table 1). Aplite and amphibolite rock masses possessed a mean fracture spacing of 0.37 m and 0.43 m, respectively. The rock mass strength (RMS) was lowest for RW3-S (62) and ranged between 70 and 77 for the other rockwalls (Table 1).

4.2 Meteorological, rock surface and rock temperature data

The meteorological station located at 2910 m recorded a MAAT between -1.1 and -0.6 °C (Table 3). In winter, mean winter air temperature (MWAT) ranged from -6.5 to -9.1°C, while mean summer air temperature (MSAT) was 5.9 to 6.8 °C in summer. Snow cover ranged between 216 and 246 days (Fig. 3a), onset was around mid-November and snow cover lasted until mid-June. Recorded snow depth on flat terrain reached between 157 and 371 cm (Table 3). Rock surface temperatures (RST) followed the annual and daily oscillation of air temperatures (Fig. 3b-g). The MARST showed no clear altitudinal trend with decreasing temperatures at higher locations as expected from air temperature trends (Table 3). South-facing rockwalls revealed warmer MARST than north-facing rockwalls and ranged between 2.2 and 2.5 °C at RW1 at 3157 m and between 4.6 and 6 °C at RW3 at approximately 2700 m. The altitudinal difference between north and south-facing loggers at RW3 is 50 m, which corresponds to 0.3°C colder conditions at the higher located south-facing rockwall. At north-facing rockwalls, mean winter rock surface temperature (MWRST) showed an increase with decreasing altitude. South-facing rockwalls showed 0.5 to 1.6 °C warmer winter conditions than north-facing rockwalls, however the logger located at RW3-S recorded -1.8° C colder temperatures in 2017/18 than RW3-N. Mean summer rock surface temperature (MSRST) showed no elevation pattern and highest values were recorded at RW1-N. South-facing rockwalls revealed 1.9 to 2.1 °C warmer conditions at RW1 that increased to 8.5 to 8.6 °C difference at RW3.

The annual temperatures of north-exposed rockwalls revealed an amplitude increase with increasing altitude (Fig. 3 b, d, f-g), which was between -7.0 °C to 13.9 °C at RW4 at 2580 m and -15.6 °C and 17.6 °C at RW1-N at 3157 m. The annual temperature amplitude was increased at south-facing rockwalls and was between -17.8 °C and 29.4 °C at RW1-S and -12 °C and 32 °C at RW3-S. At daily scale, loggers at north-facing rockwalls measured small daily temperature variations up to 4 °C, whereas loggers at south-exposed rockwalls recorded variations up to 16.5 °C. Snow cover attenuated daily temperature oscillations with expected high deviation between north- and south-exposed rockwalls. At north-facing rockwalls, snow cover started between October and December and lasted between 220 days and 251 days (RW2) per year with only minor differences between RW2 to RW4 and individual years (Fig. 3d, f, g). An exception was the highest rockwall RW1-N with only 120 to 160 days (Fig. 2b). At south-facing rockwalls, snow onset was delayed to mid-November and February and snow cover duration was reduced to 138 to 164 days at RW1-S and between 5 and 85 days at RW3-S (Fig. 3 c, e).

The thermal offset is characterized as the temperature difference between measured 10-day average rock surface temperature and modelled 10-day average air temperature adjusted to rockwall altitude. RST at south-facing rockwalls are usually warmer than air temperature during snow-free periods resulting in a positive thermal offset (Fig. 3c, e). At north-facing rockwalls, the thermal offset fluctuated around zero during snow-free periods (Fig. 3 b, d, f-g). Following snow onset, the thermal offset was positive indicating warmer RST than air temperature. The thermal offset reversed to negative temperatures at half or two third of the snow cover period and RST were colder than air temperatures.

Temperature regimes inside our rockwalls showed a typical attenuated and shifted development of RST with warmest and coldest temperatures at the surface (Fig. S1). The results revealed that positive temperatures reached seasonally down to 2.5 m depths at RW2 and to 3.5 m at RW1-N, while the rock mass below showed continuous negative rock temperatures for the entire study period (Fig. S1a, c). In contrast, south-facing and lower elevated north-facing rockwalls experienced seasonal freezing, while rock temperatures below 1.2 and 5.5 m depths, respectively, remained positive throughout the measurement period (Fig. S1 b, d-f). Maximum summed temperature gradients at north-facing rockwalls reached from 95 to 175 °C dm^{-1} at the surface. In contrast, south-facing rockwalls revealed higher maximum temperature gradients between 377 °C dm^{-1} (RW1-S) and 816 °C dm^{-1} (RW3-S).

4.3 Frost cracking model results

The HR-Model showed largest frost cracking between 1.17 and 1.32 °C-day dm^{-1} at RW1-S and between 1.53 and 1.71 °C-day dm^{-1} at RW3-S at south facing rockwalls (Fig. 4 a, m, Fig. 6a). The frost cracking maximum was located at (0.1 m) or near the surface (0.1 – 0.3 m). Frost cracking affected the rock mass down to 0.9 and 1.8 m rock depth (Table 4). North-facing rockwalls revealed a decrease of frost cracking and frost penetration depth with increasing altitude (Fig, 4 e, i, q, u, Fig. 6a, Table 4). Frost cracking peaks were reached at the surface. The A-Model showed an identical pattern of frost cracking, however, the magnitude of modelled frost cracking was reduced by 65 to 80 % on south facing rockwalls (Fig. 4 b, n) and slightly on north facing rockwalls (Fig. 4f, j, r, v, Fig. 6b, Table 4).

The WH-model revealed highest modelled crack lengths at RW1-S with 0.27 to 0.38 m and RW1-N with 0.16 to 0.17 m located at approximately 3157 m (Fig. 6c). The peak of frost cracking was reached at a depth between 0.8 and 0.9 m on the south-facing rockwall and between 0.3 to 1.1 m on the north facing rockwall and affected the rockwall up to 1.8 m depth at RW1-S and 3.3 m at RW1-N (Fig. 4c, g, Table 4). RW2 consisting of aplite and located at 2907 m showed a lower crack length growth than RW1-N with a peak at 0.2 to 0.5 m. Frost cracking affected the rockwall to 2 m depth (Fig. 4 k). The south-facing RW3-S showed crack length growth up to 0.11 and 0.19 m with high differences between 2017/18 and 2018/19 (Fig. 4o). The peak crack length growth was reached at the surface and frost weathering penetrated 1 m into the rock mass. In contrast, RW3-N consisting of amphibolite revealed no to very low crack length growth with a maximum at the surface and a rock mass affected up to 0.4 m depth (Fig. 4s). RW4 showed frost cracking only in 2016/17 and crack length reached 0.19 m with a maximum at the surface and a penetration depth up to 1.1 m (Fig. 4w).

The R-Model revealed a frost cracking pattern similar to the WH-model (Fig. 6d). Highest frost cracking was modelled at south-facing rockwalls with in porosity change of 0.1 to 0.15 % at RW3-S and 0.07 % at RW1-S (Fig. 4d, p, Table 4). The maximum frost cracking was modelled at the surface and affected the rockwalls to a depth of 1 m at RW3-S and 1.8 m at RW1-S. North-facing rockwalls RW1-N and RW2 revealed a porosity change of 0.02 to 0.03 % with a maximum at the surface but also a second peak between 0.3 or 0.9 m rock depth. Frost cracking affected the rockwalls to depth between 1.3 and 1.7 m (Fig. 4 h, l). RW3-N consisting of amphibolite showed no frost cracking at all, while frost cracking at RW4 was minimum (0.01 %) with a low penetration depth of 0.2 m and the maximum at the surface (Fig. 4x).

4.4 Sensitivity analysis

We tested the sensitivity of the used frost cracking models for rock thermal diffusivity, hydraulic properties, initial crack length and fracture toughness. Rock thermal conductivity and specific heat capacity varies largely within rock types and we used end members of calculated rock thermal diffusivity. Decreasing the rock diffusivity shifted the modelled frost cracking pattern in in all used models. The magnitude of frost cracking was amplified, however, the peak depth was shifted closer to the surface and the penetration depth was reduced (Fig. 5 a-d, Fig. S2 in the supporting info). Increasing the rock thermal diffusivity resulted in a decrease of frost cracking magnitude, slightly reduced the penetration depth and shifted the frost cracking peak. Increasing the hydraulic conductivity from 5 x 10^{-14} m s^{-1} to 5 x 10^{-10} m s^{-1} and hydraulic permeability from 10^{-18} to 10^{-14} m^2 increased the frost cracking magnitude of the WH- and R-Model, while penetration depth and peak location was maintained (Fig. 5e-f, Fig. S3 in the supporting information). In WH-model, the four-order of magnitude increase of hydraulic conductivity resulted in an increase of crack length growth by two to three orders of magnitude. In contrast, the hydraulic permeability increase by four orders of magnitude shifted the porosity change in the R-model by the same order of magnitude.

Applying a decreased initial crack length of 0.01 m instead of 0.1 m, the frost cracking was decreased to zero in the WH- and R-model (Fig. 5g-h, Fig. S4 in the supporting information).). Only at RW1-N, the WH-model showed a minor frost cracking activity. For sensitivity analysis of fracture toughness, we used maximum and minimum end members for each rock type. Increasing the fracture toughness shifted the modelled frost cracking pattern in WH- and R-model with a reduced magnitude, a peak closer to surface and reduced penetration depth (Fig.5 i-j, Fig. S5 in the supporting information). In contrast, decreasing fracture toughness resulted in a frost cracking shift with frost cracking magnitude increase, a peak located at higher depth and deeper frost cracking penetration.

5 Discussion

5.1 Thermal regime of the rockwalls

Air temperatures are influenced by elevation, however, rock surface temperatures additionally depend on topography, snow cover, fracturing and water availability. Our north-facing rockwalls demonstrate that MARST, MWRST and MSRST show no clear altitudinal trend with decreasing temperatures at higher locations as expected from air temperature trends (Table 3). In addition, rock surface temperatures revealed an annual variation that increased with altitude at north-exposed rockwalls and was amplified at south-facing rockwalls (Fig. 3b-g). RST revealed higher temperatures at RW1 than RW2, which we interpret as a result of increased solar radiation on the ridge (Fig. 1d) compared to shaded location at RW2 within the Rothorn cirque (Fig. 1e), therefore, the altitudinal pattern is disturbed by shading effects due to topography as previously observed by several studies [e.g. *Haberkorn et al.*, 2015a]. Daily temperature variation increased from north-facing rockwalls with 4°C variation up to 16.5 °C at south-exposed rockwalls. We interpret this behavior as a result of topography that changes the insolated geometry and results in solar radiation differences [*Gruber et al.*, 2004; *Hasler et al.*, 2011b].

Our rock temperature data showed 2.2 to 2.5 °C warmer MARST at south-facing rockwalls to north-facing rockwalls at RW1, which even increased to 4.6 to 6.0 °C at RW3 (Table 3). Rockwalls at RW1 are located on approximately identical elevation, while RW3-S is located 50 m above RW3-N, which corresponds to a 0.3°C temperature decrease based on the calculated lapse rate of 6°C km^{-1}. This would even increase the observed temperature difference. The measured MARST differences are within the range of previously observed aspect-induced differences that ranged between 3.3 to 3.8 °C at Gemsstock [*Haberkorn et al.*, 2015a], up to 3.9 °C at the Steintaelli in 2012-2014 [*Draebing et al.*, 2017a] and up to 5 °C in partly snow covered rockwalls at Aiguille du Midi [*Magnin et al.*, 2015], Matterhorn and Jungfraujoch [*Hasler et al.*, 2011b]. Several authors observed also an increase of MARST differences up to 7 °C in snow-free rockwalls [*Gruber et al.*, 2004; *Hasler et al.*, 2011b]. These large MARST differences results in permafrost occurrence on the north-facing RW1, while RW1-S is permafrost-free as demonstrated by geophysical measurements between 2006 to 2019 [*Draebing et al.*, 2017a; *Krautblatter & Draebing*, 2014; *Scandroglio et al.*, 2021]. Our recorded aspect-induced temperature differences correspond to an altitude between 350 and 1000 m assuming a temperature lapse rate of 0.6 °C km^{-1} and demonstrate that MAAT adjusted to altitudes will fail completely to simulate the influence of aspect.

Snow cover in rockwalls is highly variable due to topographic effects such as slope angle, distance to rock ledges and wind drift [*Haberkorn et al.*, 2015a; *Wirz et al.*, 2011]. Our logger data revealed a decreased snow duration at RW1-N at 3157 m, (120 to 161 days) compared to lower-elevated RW2, RW3-N and RW4 (>207 days; Table 3 and Fig. 3). RW1 also experienced a delayed onset of snow cover, which can be result of less topographic shading and enhanced solar radiation at ridge locations [*Haberkorn et al.*, 2015a], steeper rockwalls and a longer required snow accumulation time from the below laying ledge slope upwards as observed previously in the Steintaelli [*Draebing et al.*, 2017a]. Less snow cover at RW1-N enabled more cooling in winter (Fig. 2b). Our data demonstrated an earlier snowmelt at RW1-N compared to RW2-RW4 especially in 2018/19 (Fig. 2), which we interpret as a result of increased insolation at the ridge location. At north-facing rockwalls, the thermal offset fluctuated around zero during snow-free periods (Fig. 3 b, d, f-g), however, the thermal offset was positive indicating warmer RST than air temperature following snow onset. This indicates that snow cover had a warming effect on rockwall temperatures [*Draebing et al.*, 2017a; *Luetschg et al.*, 2008]. A delayed snow onset as observed at RW1-N results in increased cooling of the rockwall. The thermal offset reversed to negative temperatures at half or two third of the snow cover period, therefore, RST were colder than air temperatures and snow had a cooling effect [*Draebing et al.*, 2017a; *Luetschg et al.*, 2008]. In summary, insolation and insulation controls the effect of air on rock surface temperature. The insulation effect can be decreased in very steep cliffs due to decreased or lack of snow cover. Frost weathering approaches using an elevation-adjusted MAAT with uniform half amplitudes for annual or daily oscillation fail to model the thermal regime adequately [e.g. *Delunel et al.*, 2010; *Hales & Roering*, 2009; *Scherler*, 2014]. *Anderson et al.* [2013] already stated that frost cracking models should take the radiation field and non-uniform snow cover more realistically into account, thus, these effects results in complex RST histories. By using measured RST, we are able to integrate these complexities into our frost cracking model approach.

5.2 Sensitivity of frost cracking models to thermal, hydraulic and mechanical properties

5.2.1 Influence of thermal parameters and thermal processes on frost cracking

The thermal regime was modelled based on assumptions on heat transport, porosity and water infill, which vary spatially and temporally and cannot be better resolved by existing model approaches. The investigated rockwalls comprising schisty quartz slate are highly anisotropic resulting from rock fabric (0.55) compared to isotropic amphibolite (0.05) and aplite (0.06) [*Draebing & Krautblatter*, 2019]. However, the heat transport model assumes an isotropic rock. The rock mass of rockwalls comprise fractures, which are incorporated into the heat transport model by increasing porosity from below 1% to 3% (Table 2), which is the common way to incorporate fractures in conductive heat models [*Noetzli & Gruber*, 2009; *Noetzli et al.*, 2007; *Wegmann*, 1998]. An increased water-filled porosity will significantly increase the lag of heat transport due to latent heat processes [*Wegmann*, 1998]. In addition, fractures increase vertical groundwater flow [*Dietrich et al.*, 2005; *Forster & Smith*, 1989] and associated advective heat transport [*Draebing et al.*, 2014; *Gruber & Haeberli*, 2007] as well as convective heat transport by wind [*Gischig et al.*, 2011a, 2011b; *Moore et al.*, 2011], which are neglected in the conductive heat transport model. Therefore, the application of heat models to anisotropic rocks and rock masses can result in over- or underestimation of rock temperatures. In high-alpine rockwalls, heat transport is effected by topography and heat transport from warmer south to colder north rockwalls [*Noetzli et al.*, 2007]. These 3D-effects can be incorporated on individual mountain peaks, however, these processes cannot be resolved by 1D-model approaches or incorporated to frost weathering models working on larger geomorphic scales as landscapes [e.g. *Hales & Roering*, 2007; *Rempel et al.*, 2016].

Rock thermal diffusivity varies within rock types and between rockwalls. All frost cracking models showed a sensitivity to thermal diffusivity. Decreasing the thermal diffusivity decreased the frost cracking magnitude but increased the penetration depth (Fig. 5a-d and Fig. S2 in the supporting information). In contrast, an increased diffusivity increased the frost cracking magnitude but decreased the affected depth within the rock mass. All models used a temperature gradient in their frost cracking simulation. Our data revealed that maximum summed temperature gradients at the surface of south-facing rockwalls were between 372 °C dm^{-1} (RW1-S) and 816 °C dm^{-1} (RW3-S) and more than two times larger than temperature gradients at north-facing rockwalls, which ranged from 95 to 175 °C dm^{-1}. Higher temperature gradients result in higher frost cracking intensity for the HR- and A-model [*Anderson et al.*, 2013; *Hales & Roering*, 2007]. In the WH-model, increased temperature gradients amplify water migration towards the freezing front by decreasing flow resistance [see Eq. A-2 in *Walder & Hallet*, 1985]. Therefore, ice lenses growth is amplified and can develop higher ice pressure. In the R-model, the square of the temperature gradient is used to calculate the porosity change [see Eq. 7 in *Rempel et al.*, 2016], therefore, the influence of conductivity is increased in this model. In summary, the dependence on temperature gradient explains the higher frost cracking intensity in all models at south-facing rockwalls (Fig. 4 and 6). The range of thermal regime, where frost cracking occurs, plays a major control on the frost weathering model. The HR- and A-model apply a strict temperature range called frost cracking window between -8 to -3°C. This range corresponds with laboratory measurements of frost cracking on high porosity Berea sandstone [*Hallet et al.*, 1991], however, laboratory and field measurements of acoustic emissions demonstrated that frost cracking occurred as soon alpine rocks froze [*Amitrano et al.*, 2012; *Duca et al.*, 2014; *Girard et al.*, 2013]. Field measurements also observed frost cracking occurring at temperatures down to -15° [*Amitrano et al.*, 2012; *Girard et al.*, 2013] and no temperature cut off. In contrast, the WH- and R-model incorporate hydraulic and mechanical factors into their models that control the temperature limits of frost cracking.

5.2.2 Influence of water availability on frost cracking

The occurrence of water is a prerequisite for frost weathering and all used models assume saturated conditions. Rock moisture measurements in intact rock showed that rocks are not fully saturated and moisture fluctuates in the upper 0.2 m during the year [*Girard et al.*, 2013; *Sass*, 2005a]. The moisture fluctuation is influenced by moisture percolation through the fracture network [*Dietrich et al.*, 2005; *Forster & Smith*, 1989; *Girard et al.*, 2013] and by distance to snow fields that contribute moisture during snow melt [*Girard et al.*, 2013; *Sass*, 2005a]. Moisture simulations suggest that slope angle and lithology can cause differences in pore water saturation [*Rode et al.*, 2016]. Therefore, results from all frost cracking model represent the maximum scenario of frost cracking. Fractures increase not only permeability of rocks and access of water but enhance chemical and biological activity in the subsurface, which can weaken rock and therefore amplify further cracking [Anderson et al., 2013].

The HR-model assumes the availability of water from the surface or from groundwater in 20 m depth (in our model 10 m depth), when rock temperatures are positive. Therefore, our model results showed lowest frost cracking activity in permafrost affected rockwalls (RW1-N and RW2, Fig. 4 e, i), where rock temperatures at 10 m are negative throughout the year (Fig. S1a, c in the supporting information). Our model results using the A-model revealed 65 to 80 % lower frost cracking activity in south-facing rockwalls and slightly lower frost cracking at north-facing rockwalls. The model assumes water available along rock depths with positive temperatures, however, penalizes water transport, which reduced the frost cracking activity. *Anderson et al.* [2013] stated that penalization is a simplification and no true assessment of water availability. Water in rock can be present even in frozen rocks [*Mellor*, 1970], however, the water preconditions of the A-model resulted in low or no frost cracking at permafrost affected rockwalls RW1-N and RW-2 (Fig. 4f, j).

The WH- and R-Model assume saturated conditions but use hydraulic conductivity or permeability at the pore freezing point to reduce water availability. Unfrozen permeability varies by six orders of magnitude [*Rempel et al.*, 2016] and applying a sensitivity test of hydraulic permeability and conductivity with endmembers differing by four orders of magnitude demonstrate a high sensitivity of both models. The frost cracking magnitude increased between two and three orders in the WH- and four orders in the R-model (Fig. 5e-f and Fig. S3 in the supporting information), however depth and location of magnitude pattern is persistent. Therefore, the magnitude of frost cracking can only be interpreted in a qualitative way, however, the depth pattern can be quantitatively compared to fracture spacing and rock strength. Hydraulic properties are affected by curvature effects and influenced by pore size, grain size and ice-liquid surface energy, which are poorly constrained and vary at geomorphic scales such as rockwalls. Our model results of WH- and R-models revealed intense frost cracking in the permafrost-affected rockwalls RW1-N and RW2 (Fig. 4 g-h, k-l). *Murton et al.* [2006] used the model by *Walder and Hallet* [1985] to model frost cracking in high porosity and isotropic permafrost-affected Tuffeau limestone samples and the modelled cracking lengths reflected well observed crack clustering. *Walder and Hallet* [1985] use a generalized Darcy’s law with a constant hydraulic conductivity k_{hc} of 5×10^{-14} m s^{-1} based on sediments and soils. In contrast, *Rempel et al.* [2016] determine their lower boundary of frost cracking by integrating permeability in form of a simple power-law approximation. Both approaches results in frost cracking activity in temperature ranges from -1 up to -15 °C, which are in better accordance to field measurements [*Amitrano et al.*, 2012; *Girard et al.*, 2013].

5.2.3 Influence of initial crack length and fracture toughness

The problem of cracking is associated with initial conditions associated with rock structure [*Anderson et al.*, 2013]. Cracks can be generated by tectonic stress [*Molnar et al.*, 2007], paraglacial stress release [*Grämiger et al.*, 2017; *Grämiger et al.*, 2020] and internal stress distribution [*Leith et al.*, 2014a, 2014b] following glacier retreat or surface processes [*Clarke & Burbank*, 2010, 2011]. Cracks also develop progressively [*Walder & Hallet*, 1985], therefore, initial conditions will be far away from assumed constant cracks. The WH- and R-models are sensitive to initial crack length and decreasing crack length by one order of magnitude reduced frost cracking to zero or almost zero at RW1-N (Fig. 5g-h, Fig. S4 in the supporting information).

The WH- and R-models are sensitive to fracture toughness as our model results demonstrated a decrease of frost cracking magnitude with a peak closer to the surface and reduced penetration depth as fracture toughness increases (Fig.5 i-j, Fig. S5 in the supporting information). In contrast, decreasing fracture toughness increased the frost cracking magnitude, shifted the peak to higher depth and increased penetration depth. *Walder and Hallet* [1985] incorporate fracture toughness by increasing the length of penny-shaped cracks when ice pressure reached a third of fracture toughness. Since frost cracking starts as ice pressure approaches the rock strength and ice pressure development depends on temperature, each rock type has an individual strength-dependent frost cracking temperature range [*Walder & Hallet*, 1985], which is supported by laboratory and field studies [*Draebing & Krautblatter*, 2019; *Draebing et al.*, 2017b; *Murton et al.*, 2006]. Therefore, frost cracking is enhanced at RW1-N, RW1-S, RW3-S and RW-4 (Fig. 4 g-i), where low-strength schisty quartz slate (1.66 MPa $m^{1/2}$) is abundant, in contrast to higher strength aplite (1.87 MPa $m^{1/2}$) at RW2 and amphibolite (2.19 MPa $m^{1/2}$) at RW3-N.

The upper boundary of the R-model is calculated based on fracture toughness and crack length. This upper temperature limit of frost cracking increases from amphibolite to aplite and schisty quartz slate due to decreasing K_C and increases with increasing crack length (Fig. S6 in the supporting information). Therefore, large cracks are more easily propagated than small cracks, which is in accordance to studies on fracture mechanics [*Atkinson & Rawlings*, 1981; *Erismann & Abele*, 2001]. Crack length is assumed uniform during modelling and frost weathering is expressed as porosity increase, therefore, a progressive fracture propagation with time that increases effective porosity and enhances fluid flow is ignored. Due to higher strength of amphibolite, no frost cracking occurs at all at RW3-N, while lower strength schisty quartz slate rocks are easier to crack.

5.3 Topographic pattern of frost cracking in the Hungerli

All models showed highest frost cracking activity at south-facing rockwalls, however, the fracture spacing and rock strength measurements cannot support the resulting frost cracking patterns. Highest overall frost cracking was measured at RW1-S and affected the upper 1 m in the R-model and upper 1.8 m in the HR-, A- and WH-models (Fig. 4a-d). However, fracture spacing showed variation between 1.65 m and 2.98 m with an average spacing of 2.82 m (Fig. 6e), therefore, fracture spacing is larger than the effect of frost cracking depth and is not corresponding to the model results. Except the WH-model, all models revealed a peak frost cracking at the surface. Repetitive frost cracking activity reduces both compressive and tensile strength of rocks [*Jia et al.*, 2021; *Jia et al.*, 2015], therefore, a frost cracking peak at the surface should result in lowering the rock strength due to rock breakdown. However, Schmidt hammer measurements at RW1-S showed highest measured rebound values (53) of schisty quartz slate rocks (Fig. 6f), which is contrary to the modelled frost cracking patterns. The rebound value could be increased if fresh rock is exposed following a rockfall, however, a fresh rockfall scar was not visible at RW1-S or any other logger location.

Model results from RW3-S showed high frost cracking rates (Fig. 6a-d) with an affected rock mass of 0.5 m in the R-model, 0.9 m in HR- and A-models and 1m in the WH-model (Fig. 4e-h). Fracture spacing varied between 0.1 and 0.41 m with a mean of 0.32 m (Fig. 6f) which corresponds best with the R-model. Frost cracking showed highest magnitudes at surface at all models and mean rebound values were the lowest measured values in the Hungerli (31). While fracture spacing are smaller than frost cracking activity, which can result von tectonics or other processes, the Schmidt hammer value corresponds to a high weathering activity at the surface. However, RW3-S experienced highest daily thermal variation, which can increase thermal stresses [*Eppes et al.*, 2016] that can support near surface rock breakdown and, therefore, the low rock strength can be a result of other weathering processes than frost weathering. Field observations using rockfall collectors and talus deposits recorded significant more frost weathering associated rockfall at north-facing than south-facing rockwalls [*Sass*, 2005b, 2007], however, frost cracking models revealed highest magnitudes at south-facing rockwalls. The contrary model patterns of RW1-S and RW3-S can be a result of unrealistic rock moisture assumptions at south-facing rockwalls. Due to higher insolation, south-facing rockwalls have lower moisture contents near to the surface [0.2 m; *Rode et al.*, 2016; *Sass*, 2005a] where highest frost cracking magnitudes were modelled. Therefore, moisture conditions are contrary to assumed saturated conditions in the frost cracking model set up. However, there is no study yet that provides information on aspect-induced rock moisture variation below 0.2 m, which would enable an improvement of used model assumptions.

The permafrost affected rockwalls RW1-N and RW2 showed contrary results between purely thermal models (HR and A-model) and thermo-mechanical models (WH- and R-model). At RW1-N, frost cracking effects were limited to the upper 0.1 to 0.2 m of the rockwall in the HR- and A- model with peaks at the surface (Fig. 4e-f, i-j). We interpret this frost cracking pattern as a result from the water availability assumptions (see Chapter 5.2.2). In contrast, WH- and R-models revealed high frost cracking intensities. The WH-model showed an effected rock mass of 3.1 m with peak intensity at 0.3 to 1.1 m (Fig. 4g), while the R-model revealed a penetration depth of 1.7 m with peaks between 0.1 and 0.9 m (Fig. 4h). These model results correspond to measured fracture spacing that ranged between 0.24 to 1.16 m with an average of 0.85 m (Fig. 6f). Schmidt hammer values at RW1-N were 46 and suggest a hard rock strength due to low frost cracking intensity at the surface (Fig. 6e). RW2 showed a similar pattern with decreased penetration depth to 1.3 m in the R-model and 2 m in the WH-model and peaks at 0.1 to 0.3 m and 0.2 to 0.5 m, respectively. Model results correspond to measured fracture spacing that varied between 0.12 and 0.5 m with an average of 0.37 m (Fig. 6f). Rebound values of the aplite rockwall were 40, which suggests less frost cracking at the surface and corresponds better with WH-model results.

RW3-N consists of high-strength amphibolite characterized by high rebound values of 64. The R-model showed no frost cracking and WH- model only minor frost cracking limited to the upper 0.4 m in 2016/17 (Fig. 6s-t), which we interpret as a result of insufficient ice pressure development that were unable to exceed the rock strength thresholds of the models. In contrast, the A-model showed highest frost cracking on north-facing rockwalls and the HR-model slightly lower magnitudes (Fig. 4q-r, Fig. 6a-b). Frost cracking intensity peaked at the surface and reached to 0.7 m. Fracture spacing ranged from 0.13 to 0.52 m with a mean spacing of 0.43 m that corresponds with HR-, A- and WH-model results. However, the observed peaks at the surface especially of the A- and HR-model are contrasting to the highest measured rebound values of 64. RW4 consisting of schisty quartz slate showed highest frost cracking intensities at HR- and WH-models and lower intensities at A- and R-models (Fug. 4 u-x). Fracture spacing ranged from 0.21 to 1 m with 0.67 m on average (Fig. 6f), which corresponds better to A-, HR- and WH-models (Table 4) than the R-model that showed only minor penetration depth of 0.2 m. The low measured rebound value of 39 supports the occurrence of high intensities at surface simulated by all models.

Excluding the anomalous high frost cracking intensities on south-facing rockwalls in the analysis (Fig. 6), the north-facing rockwalls in the Hungerli Valley experience a topographic pattern of frost cracking with increasing frost cracking with decreasing altitude in the HR- and A-model and a contrary increasing frost cracking activity with increasing altitude in the WH- and R-models (Fig. 6). Fracture spacing and Schmidt hammer values suggest a higher correspondence of WH- and R-models. In the calcareous Alps, field observations recorded an increased rockfall activity at higher location using rockfall collectors [*Sass*, 2005b] and using lichenometry on talus slopes [*Sass*, 2010]. *Sass* [2005b, 2010] suggested that the observed rockfall increase along altitude was associated with permafrost increased frost weathering. Therefore, field studies support the observed frost cracking patterns of the WH- and R-models and contradicts model results by HR- and A-model.

6 Conclusions

In high alpine rockwalls, topography controls the thermal regime by changing insolation and insulation. Consequently, a thermal offset between air temperature and rock surface temperature exists that complicate an air temperature based frost cracking model approach. Frost weathering depends on the thermal regime, water availability and mechanical rock properties. Our sensitivity analysis demonstrate that thermo-mechanical models are very sensitive to hydraulic parameters and frost cracking changes orders of magnitude, while the models are less sensitive to mechanical and thermal parameters. As a result of the sensitivity the frost cracking magnitude changes, however, the spatial frost cracking patterns within the rock mass including the peak locations are consistent. All frost cracking models experienced highest frost weathering at south-facing rockwalls, which is contrary to measured fracture and rock strength properties of these rockwalls and to results of previous field studies. We suggest that this is a result of overestimated rock moisture availability, which would reduce frost weathering and should be investigated in future research. Purely thermal models underestimate the frost cracking intensity in permafrost-affected rockwalls due to their water-availability constraints. In contrast, thermo-mechanical models incorporate hydraulic permeability or conductivity and show highest frost cracking in permafrost-affected rockwalls, which is consistent to observed fracture and rock strength patterns. Thermo-mechanical models revealed a topographic altitudinal frost cracking pattern with increasing frost weathering intensity with increasing altitude, while purely thermal models developed an inverse related topographic frost cracking pattern with highest intensities at lower elevations. In summary, thermo-mechanical models produced more realistic frost weathering patterns on rockwalls and along topographic gradients in the Hungerli Valley than purely thermal models.

Acknowledgments, Samples, and Data

Daniel Draebing received funding from the German Research Foundation (DR1070/1-1). We thank Arne Thiemann, Arne Brandschwede, Florian Strohmaier and Sam McColl for fieldwork support. The authors acknowledge laboratory support at Technical University of Munich by Fritz Ettl, Heiko Käsling and Georg Stockinger. The authors thank the editor Amy West, associated editor Matthew Bain, Jill Marshal and two anonymous reviewers for their comments that helped to significantly improve the manuscript. Furthermore, Daniel Draebing thanks Michael Krautblatter and Maarten Kleinhans for hospitality. All datasets for this research are available at doi: 10.6084/m9.figshare.14178539.

References

Amitrano, D., Gruber, S., & Girard, L. (2012). Evidence of frost-cracking inferred from acoustic emissions in a high-alpine rock-wall. *Earth and Planetary Science Letters, 341*, 86-93. doi:10.1016/j.epsl.2012.06.014

Andersland, O. B., & Ladanyi, B. (2004). *Frozen ground engineering*. Hoboken: John Wiley & Sons.

Anderson, R. S. (1998). Near-surface thermal profiles in alpine bedrock: Implications for the frost weathering of rock. *Arctic and Alpine Research, 30*(4), 362-372. doi:10.2307/1552008

Anderson, R. S., Anderson, S. P., & Tucker, G. E. (2013). Rock damage and regolith transport by frost: an example of climate modulation of the geomorphology of the critical zone. *Earth Surface Processes and Landforms, 38*(3), 299-316. doi:10.1002/esp.3330

Atkinson, B. K. (1984). Subcritical crack growth in geological materials. *Journal of Geophysical Research: Solid Earth, 89*(B6), 4077-4114. doi:10.1029/JB089iB06p04077

Atkinson, B. S., & Rawlings, R. D. (1981). Acoustic Emission During Stress Corrosion Cracking in Rocks. In D. W. Simpson & P. G. Richards (Eds.), *Earthquake Prediction* (pp. 605-616). doi:10.1029/ME004p0605

Bearth, P. (1980). *Geologischer Atlas der Schweiz 1:25000. Erläuterungen zum Atlasblatt 71 (1308 St. Niklaus)*. Basel: Schweizer Geologische Kommission.

Carslaw, H. S., & Jaeger, J. C. (1986). *Conduction of heat in solids* (2nd ed.). Oxford: Clarendon Press.

Cermák, V., & Rybach, L. (1982). Thermal conductivity and specific heat of minerals and rocks. In G. Angeneister (Ed.), *Landolt–Börnstein Zahlenwerte and Funktionen aus*

Naturwissenschaften und Technik, Neue Serie, Physikalische Eigenschaften der Gesteine (V/1a) (pp. 305–343). Berlin: Springer.

Chang, S.-H., Lee, C.-I., & Jeon, S. (2002). Measurement of rock fracture toughness under modes I and II and mixed-mode conditions by using disc-type specimens. *Engineering Geology, 66*(1–2), 79-97. doi:10.1016/S0013-7952(02)00033-9

Clarke, B. A., & Burbank, D. W. (2010). Bedrock fracturing, threshold hillslopes, and limits to the magnitude of bedrock landslides. *Earth and Planetary Science Letters, 297*(3–4), 577-586. doi:10.1016/j.epsl.2010.07.011

Clarke, B. A., & Burbank, D. W. (2011). Quantifying bedrock-fracture patterns within the shallow subsurface: Implications for rock mass strength, bedrock landslides, and erodibility. *Journal of Geophysical Research: Earth Surface, 116*, F04009. doi:10.1029/2011jf001987

Delunel, R., van der Beek, P. A., Carcaillet, J., Bourles, D. L., & Valla, P. G. (2010). Frost-cracking control on catchment denudation rates: Insights from in situ produced Be-10 concentrations in stream sediments (Ecrins-Pelvoux massif, French Western Alps). *Earth and Planetary Science Letters, 293*(1-2), 72-83. doi:10.1016/j.epsl.2010.02.020

Dietrich, P., Helmig, R., Sauter, M., Hötzl, H., Köngeter, J., & Teutsch, G. (2005). *Flow and Transport in Fractured Porous Media*. Berlin: Springer.

Dietze, M., Turowski, J. M., Cook, K. L., & Hovius, N. (2017). Spatiotemporal patterns, triggers and anatomies of seismically detected rockfalls. *Earth Surface Dynamics, 5*(4), 757-779. doi:10.5194/esurf-5-757-2017

Draebing, D., Haberkorn, A., Krautblatter, M., Kenner, R., & Phillips, M. (2017a). Thermal and Mechanical Responses Resulting From Spatial and Temporal Snow Cover Variability in Permafrost Rock Slopes, Steintaelli, Swiss Alps. *Permafrost And Periglacial Processes, 28*(1), 140-157. doi:10.1002/ppp.1921

Draebing, D., & Krautblatter, M. (2012). P-wave velocity changes in freezing hard low-porosity rocks: a laboratory-based time-average model. *The Cryosphere, 6*, 1163-1174. doi:10.5194/tc-6-1163-2012

Draebing, D., & Krautblatter, M. (2019). The Efficacy of Frost Weathering Processes in Alpine Rockwalls. *Geophysical Research Letters, 46*(12), 6516-6524. doi:10.1029/2019gl081981

Draebing, D., Krautblatter, M., & Dikau, R. (2014). Interaction of thermal and mechanical processes in steep permafrost rock walls: A conceptual approach. *Geomorphology, 226*, 226-235. doi:10.1016/j.geomorph.2014.08.009

Draebing, D., Krautblatter, M., & Hoffmann, T. (2017b). Thermo-cryogenic controls of fracture kinematics in permafrost rockwalls. *Geophysical Research Letters, 44*(8), 3535-3544. doi:10.1002/2016GL072050

Duca, S., Occhiena, C., Mattone, M., Sambuelli, L., & Scavia, C. (2014). Feasibility of Ice Segregation Location by Acoustic Emission Detection: A Laboratory Test in Gneiss. *Permafrost And Periglacial Processes, 25*(3), 208-219. doi:10.1002/ppp.1814

Eppes, M.-C., & Keanini, R. (2017). Mechanical weathering and rock erosion by climate-dependent subcritical cracking. *Reviews of Geophysics, 55*(2), 470-508. doi:10.1002/2017RG000557

Eppes, M. C., Magi, B., Hallet, B., Delmelle, E., Mackenzie-Helnwein, P., Warren, K., & Swami, S. (2016). Deciphering the role of solar-induced thermal stresses in rock weathering. *Geological Society of America Bulletin, 128*(9-10), 1315-1338. doi:10.1130/b31422.1

Erismann, T. H., & Abele, G. (2001). *Dynamics of Rockslides and Rockfalls*. Heidelberg: Springer.

Fahey, B. D., & Lefebure, T. H. (1988). The freeze-thaw weathering regime at a section of the Niagara escarpment on the Bruce Peninsula, Southern Ontario, Canada. *Earth Surface Processes and Landforms, 13*(4), 293-304. doi:10.1002/esp.3290130403

Forster, C., & Smith, L. (1989). The influence of groundwater-flow on thermal regimes in mountainous terrain - a model study. *Journal of Geophysical Research-Solid Earth and Planets, 94*(B7), 9439-9451. doi:10.1029/JB094iB07p09439

Gilpin, R. R. (1979). A model of the “liquid-like” layer between ice and a substrate with applications to wire regelation and particle migration. *Journal of Colloid and Interface Science, 68*(2), 235-251. doi:10.1016/0021-9797(79)90277-7

Gilpin, R. R. (1980). Theoretical studies of particle engulfment. *Journal of Colloid and Interface Science, 74*(1), 44-63. doi:10.1016/0021-9797(80)90169-1

Girard, L., Gruber, S., Weber, S., & Beutel, J. (2013). Environmental controls of frost cracking revealed through in situ acoustic emission measurements in steep bedrock. *Geophysical Research Letters*, *40*(9), 1748-1753. doi:10.1002/grl.50384

Gischig, V. S., Moore, J. R., Evans, K. F., Amann, F., & Loew, S. (2011a). Thermomechanical forcing of deep rock slope deformation: 1. Conceptual study of a simplified slope. *Journal of Geophysical Research-Earth Surface, 116*, F04010. doi:10.1029/2011jf002006

Gischig, V. S., Moore, J. R., Evans, K. F., Amann, F., & Loew, S. (2011b). Thermomechanical forcing of deep rock slope deformation: 2. The Randa rock slope instability. *Journal of Geophysical Research-Earth Surface, 116*, F04011. doi:10.1029/2011jf002007

Grämiger, L. M., Moore, J. R., Gischig, V. S., Ivy-Ochs, S., & Loew, S. (2017). Beyond debuttressing: Mechanics of paraglacial rock slope damage during repeat glacial cycles. *Journal of Geophysical Research: Earth Surface, 122*(4), 1004-1036. doi:10.1002/2016JF003967

Grämiger, L. M., Moore, J. R., Gischig, V. S., Loew, S., Funk, M., & Limpach, P. (2020). Hydromechanical rock slope damage during Late Pleistocene and Holocene glacial cycles in an Alpine valley. *Journal of Geophysical Research: Earth Surface, 125*, e2019JF005494. doi:10.1029/2019jf005494

Gruber, S., & Haeberli, W. (2007). Permafrost in steep bedrock slopes and its temperaure-related destabilization following climate change. *Journal of Geophysical Research - Earth Surface, 112*, F02S18. doi:10.1029/2006JF000547

Gruber, S., Hoelzle, M., & Haeberli, W. (2004). Rock-wall Temperatures in the Alps: Modelling their Topographic Distribution and Regional Differences. *Permafrost And Periglacial Processes, 15*, 299-307. doi:10.1002/ppp.501

Haberkorn, A., Hoelzle, M., Phillips, M., & Kenner, R. (2015a). Snow as a driving factor of rock surface temperatures in steep rough rock walls. *Cold Regions Science and Technology, 118*, 64-75. doi:10.1016/j.coldregions.2015.06.013

Haberkorn, A., Phillips, M., Kenner, R., Rhyner, H., Bavay, M., Galos, S. P., & Hoelzle, M. (2015b). Thermal regime of rock and its relation to snow cover in steep alpine rock walls: Gemsstock, Central Swiss Alps. *Geografiska Annaler: Series A, 97*(3), 579-597. doi:10.1111/geoa.12101

Haberkorn, A., Wever, N., Hoelzle, M., Phillips, M., Kenner, R., Bavay, M., & Lehning, M. (2017). Distributed snow and rock temperature modelling in steep rock walls using Alpine3D. *The Cryosphere*, *11*(1), 585-607. doi:10.5194/tc-11-585-2017

Hales, T. C., & Roering, J. J. (2005). Climate-controlled variations in scree production, Southern Alps, New Zealand. *Geology*, *33*(9), 701-704. doi:10.1130/g21528.1

Hales, T. C., & Roering, J. J. (2007). Climatic controls on frost cracking and implications for the evolution of bedrock landscapes. *Journal of Geophysical Research-Earth Surface, 112*, F02033. doi:10.1029/2006jf000616

Hales, T. C., & Roering, J. J. (2009). A frost "buzzsaw" mechanism for erosion of the eastern Southern Alps, New Zealand. *Geomorphology, 107*(3-4), 241-253. doi:10.1016/j.geomorph.2008.12.012

Halla, C. (2013). *Bewegungsprozesse im Festgestein des Periglazials im Steintälli, Mattertal, Schweiz.* (Diploma Thesis, unpublished), Universität Bonn.

Hallet, B., Walder, J. S., & Stubbs, C. W. (1991). Weathering by segregation ice growth in microcracks at sustained subzero temperatures: Verification from an experimental study using acoustic emissions. *Permafrost And Periglacial Processes, 2*(4), 283-300. doi:10.1002/ppp.3430020404

Hasler, A., Gruber, S., Font, M., & Dubois, A. (2011a). Advective Heat Transport in Frozen Rock Clefts: Conceptual Model, Laboratory Experiments and Numerical Simulation. *Permafrost And Periglacial Processes, 22*(4), 378-389. doi:10.1002/ppp.737

Hasler, A., Gruber, S., & Haeberli, W. (2011b). Temperature variability and offset in steep alpine rock and ice faces. *The Cryosphere, 5*(4), 977-988. doi:10.5194/tc-5-977-2011

Hipp, T., Etzelmüller, B., & Westermann, S. (2014). Permafrost in Alpine Rock Faces from Jotunheimen and Hurrungane, Southern Norway. *Permafrost And Periglacial Processes, 25*(1), 1-13. doi:10.1002/ppp.1799

ISRM. (1978). Suggested Methods for the quantitative description of discontinuities in rock masses. *International Journal of Rock Mechanics and Mining Sciences & Geomechanics Abstracts*, *15*, 319-368.

Jia, H., Ding, S., Zi, F., Li, G., & Yao, Y. (2021). Development of Anisotropy in Sandstone Subjected to Repeated Frost Action. *Rock Mechanics and Rock Engineering*. doi:10.1007/s00603-020-02343-5

Jia, H., Xiang, W., & Krautblatter, M. (2015). Quantifying rock fatigue and decreasing compressive and tensile strength after repeated freeze-thaw cycles. *Permafrost and Periglacial Processes, 26*(4), 368-377. doi:10.1002/ppp.1857

Krautblatter, M. (2009). *Detection and quantification of permafrost change in alpine rock walls and implications for rock instability.* (PhD Thesis), Universität Bonn, Bonn.

Krautblatter, M., & Dikau, R. (2007). Towards a uniform concept for the comparison and extrapolation of rockwall retreat and rockfall supply. *Geogr. Ann., 89*(1), 21-40. doi:10.1111/j.1468-0459.2007.00305.x

Krautblatter, M., & Draebing, D. (2014). Pseudo 3D - P-wave refraction seismic monitoring of permafrost in steep unstable bedrock. *Journal of Geophysical Research: Earth Surface, 119*(2), 287-299. doi:10.1002/2012jf002638

Krautblatter, M., & Moore, J. M. (2014). Rock slope instability and erosion: toward improved process understanding. *Earth Surface Processes and Landforms, 39*(9), 1273–1278. doi:10.1002/esp.3578

Leith, K., Moore, J. R., Amann, F., & Loew, S. (2014a). In situ stress control on microcrack generation and macroscopic extensional fracture in exhuming bedrock. *Journal of Geophysical Research-solid Earth, 119*(1), 594-615. doi:10.1002/2012jb009801

Leith, K., Moore, J. R., Amann, F., & Loew, S. (2014b). Subglacial extensional fracture development and implications for Alpine Valley evolution. *Journal of Geophysical Research-Earth Surface, 119*(1), 62-81. doi:10.1002/2012jf002691

Lepique, M. (2008). Empfehlung Nr. 10 des Arbeitskreises 3.3 “Versuchstechnik Fels” der Deutschen Gesellschaft für Geotechnik e. V.: Indirekter Zugversuch an Gesteinsproben – Spaltzugversuch. *Bautechnik, 85*(9), 623-627. doi:10.1002/bate.200810048

Luetschg, M., Lehning, M., & Haeberli, W. (2008). A sensitivity study of factors influencing warm/thin permafrost in the Swiss Alps. *Journal Of Glaciology, 54*(187), 696-704. doi:10.3189/002214308786570881

Magnin, F., Deline, P., Ravanel, L., Noetzli, J., & Pogliotti, P. (2015). Thermal characteristics of permafrost in the steep alpine rock walls of the Aiguille du Midi (Mont Blanc Massif, 3842 m a.s.l). *The Cryosphere, 9*(1), 109-121. doi:10.5194/tc-9-109-2015

Maji, V., & Murton, J. B. (2020). Micro-computed tomography imaging and probabilistic modelling of rock fracture by freeze–thaw. *Earth Surface Processes and Landforms, 45*(3), 666-680. doi:10.1002/esp.4764

Marshall, J. A., Roering, J. J., Bartlein, P. J., Gavin, D. G., Granger, D. E., Rempel, A. W., . . . Hales, T. C. (2015). Frost for the trees: Did climate increase erosion in unglaciated landscapes during the late Pleistocene? *Science Advances, 1*(10). doi:10.1126/sciadv.1500715

Marshall, J. A., Roering, J. J., Gavin, D. G., & Granger, D. E. (2017). Late Quaternary climatic controls on erosion rates and geomorphic processes in western Oregon, USA. *Geological Society of America Bulletin, 129*(5-6), 715-731. doi:10.1130/B31509.1

Marshall, J. A., Roering, J. J., Rempel, A. W., Shafer, S. L., & Bartlein, P. J. (2021). Extensive frost weathering across unglaciated North America during the Last Glacial Maximum. *Geophysical Research Letters, n/a*(n/a), e2020GL090305. doi:10.1029/2020GL090305

Matsuoka, N. (2001). Direct observation of frost wedging in alpine bedrock. *Earth Surface Processes and Landforms, 26*(6), 601-614. doi:10.1002/esp.208

Matsuoka, N. (2008). Frost weathering and rockwall erosion in the southeastern Swiss Alps: Long-term (1994-2006) observations. *Geomorphology, 99*(1-4), 353-368. doi:10.1016/j.geomorph.2007.11.013

Matsuoka, N. (2019). A multi-method monitoring of timing, magnitude and origin of rockfall activity in the Japanese Alps. *Geomorphology, 336*, 65-76. doi:10.1016/j.geomorph.2019.03.023

Matsuoka, N., & Murton, J. (2008). Frost weathering: Recent advances and future directions. *Permafrost And Periglacial Processes, 19*(2), 195-210. doi:10.1002/ppp.620

Matsuoka, N., & Sakai, H. (1999). Rockfall activity from an alpine cliff during thawing periods. *Geomorphology, 28*, 309-328. doi:10.1016/S0169-555X(98)00116-0

Matthews, J. A., Dawson, A. G., & Shakesby, R. A. (1986). Lake shoreline development, frost weathering and rock platform erosion in an alpine periglacial environment, Jotunheimen, southern Norway. *Boreas, 15*(1), 33-50. doi:10.1111/j.1502-3885.1986.tb00741.x

McCarroll, D. (1991). The schmidt hammer, weathering and rock surface roughness. *Earth Surface Processes and Landforms, 16*(5), 477-480. doi:10.1002/esp.3290160510

McGreevy, J. P., & Whalley, W. B. (1985). Rock moisture-content and frost weathering under natural and experimental conditions - a comparative discussion. *Arctic and Alpine Research, 17*(3), 337-346. doi:10.2307/1551022

Mellor, M. (1970). *Phase composition of pore water in cold rocks.* (Vol. 292). Hanover: CRREL Research Reports.

Messenzehl, K., Viles, H., Otto, J.-C., Ewald, A., & Dikau, R. (2018). Linking rock weathering, rockwall instability and rockfall supply on talus slopes in glaciated hanging valleys (Swiss Alps). *Permafrost And Periglacial Processes, 29*(3), 135-151. doi:10.1002/ppp.1976

MeteoSwiss. (2019a). *Climate data station Grächen, 2016-2019. Provided by MeteoSwiss, the Swiss Federal Office of Meteorology and Climatology*.

MeteoSwiss. (2019b). *Climate data station Oberer Stelligletscher 2016-2019. Provided by MeteoSwiss, the Swiss Federal Office of Meteorology and Climatology*.

Molnar, P., Anderson, R. S., & Anderson, S. P. (2007). Tectonics, fracturing of rock, and erosion. *Journal of Geophysical Research: Earth Surface, 112*(F3). doi:10.1029/2005JF000433

Montgomery, D. R., & Brandon, M. T. (2002). Topographic controls on erosion rates in tectonically active mountain ranges. *Earth and Planetary Science Letters, 201*(3), 481-489. doi:10.1016/S0012-821X(02)00725-2

Moore, J. R., Gischig, V., Katterbach, M., & Loew, S. (2011). Air circulation in deep fractures and the temperature field of an alpine rock slope. *Earth Surface Processes and Landforms, 36*(15), 1985-1996. doi:10.1002/esp.2217

Murphy, B. P., Johnson, J. P. L., Gasparini, N. M., & Sklar, L. S. (2016). Chemical weathering as a mechanism for the climatic control of bedrock river incision. *Nature, 532*(7598), 223-227. doi:10.1038/nature17449

Murton, J. B., Peterson, R., & Ozouf, J. C. (2006). Bedrock fracture by ice segregation in cold regions. *Science, 314*(5802), 1127-1129. doi:10.1126/science.1132127

Mutschler, T. (2004). Neufassung der Empfehlung Nr. 1 des Arbeitskreises "Versuchstechnik Fels" der Deutschen Gesellschaft für Geotechnik e. V.: Einaxiale Druckversuche an zylindrischen Gesteinsprüfkörpern. *Bautechnik, 81*(10), 825-834. doi:10.1002/bate.200490194

Noetzli, J., & Gruber, S. (2009). Transient thermal effects in Alpine permafrost. *The Cryosphere, 3*(1), 85-99. doi:10.5194/tc-3-85-2009

Noetzli, J., Gruber, S., Kohl, T., Salzmann, N., & Haeberli, W. (2007). Three-dimensional distribution and evolution of permafrost temperatures in idealized high-mountain topography. *Journal of Geophysical Research - Earth Surface, 112*, F02S13. doi:10.1029/2006JF000545

Orr, E. N., Owen, L. A., Saha, S., & Caffee, M. W. (2019). Rates of rockwall slope erosion in the upper Bhagirathi catchment, Garhwal Himalaya. *Earth Surface Processes and Landforms, 44*(15), 3108-3127. doi:10.1002/esp.4720

Otto, J. C., Schrott, L., Jaboyedoff, M., & Dikau, R. (2009). Quantifying sediment storage in a high alpine valley (Turtmanntal, Switzerland). *Earth Surface Processes and Landforms, 34*(13), 1726-1742. doi:10.1002/esp.1856

Phillips, M., Haberkorn, A., Draebing, D., Krautblatter, M., Rhyner, H., & Kenner, R. (2016). Seasonally intermittent water flow through deep fractures in an Alpine rock ridge:

Gemsstock, central Swiss Alps. *Cold Regions Science and Technology, 125*, 117-127. doi:10.1016/j.coldregions.2016.02.010
Phillips, M., Haberkorn, A., & Rhyner, H. (2017). Snowpack characteristics on steep frozen rock slopes. *Cold Regions Science and Technology, 141*, 54-65. doi:10.1016/j.coldregions.2017.05.010
Priest, S. D. (1993). *Discontinuity Analysis for Rock Engineering*. London, Glasgow: Chapman & Hall.
Rempel, A. W., Marshall, J. A., & Roering, J. J. (2016). Modeling relative frost weathering rates at geomorphic scales. *Earth and Planetary Science Letters, 453*, 87-95. doi:10.1016/j.epsl.2016.08.019
Rode, M., Schnepfleitner, H., & Sass, O. (2016). Simulation of moisture content in alpine rockwalls during freeze–thaw events. *Earth Surface Processes and Landforms, 41*(13), 1937-1950. doi:10.1002/esp.3961
Sanders, J. W., Cuffey, K. M., Moore, J. R., MacGregor, K. R., & Kavanaugh, J. L. (2012). Periglacial weathering and headwall erosion in cirque glacier bergschrunds. *Geology, 40*(9), 779-782. doi:10.1130/g33330.1
Sass, O. (2005a). Rock moisture measurements: techniques, results, and implications for weathering. *Earth Surface Processes and Landforms, 30*(3), 359-374. doi:10.1002/esp.1214
Sass, O. (2005b). Spatial patterns of rockfall intensity in the northern Alps. *Zeitschrift für Geomorphologie, Supplementary Issues, 138*, 51-65.
Sass, O. (2005c). Temporal Variability of Rockfall in the Bavarian Alps, Germany. *Arctic, Antarctic, and Alpine Research, 37*(4), 564-573. doi:10.1657/1523-0430(2005)037[0564:tvorit]2.0.co;2
Sass, O. (2007). Bedrock detection and talus thickness assessment in the European Alps using geophysical methods. *Journal of Applied Geophysics, 62*(3), 254-269. doi:10.1016/j.jappgeo.2006.12.003
Sass, O. (2010). Spatial and temporal patterns of talus activity – a lichenometric approach in the stubaier alps, austria. *Geografiska Annaler: Series A, Physical Geography, 92*(3), 375-391. doi:10.1111/j.1468-0459.2010.00402.x
Savi, S., Delunel, R., & Schlunegger, F. (2015). Efficiency of frost-cracking processes through space and time: An example from the eastern Italian Alps. *Geomorphology, 232*, 248-260. doi:10.1016/j.geomorph.2015.01.009
Scandroglio, R., Draebing, D., Offer, M., & Krautblatter, M. (2021). 4D-Quantification of alpine permafrost degradation in steep rock walls using a laboratory-calibrated ERT approach. *Near Surface Geophysics*. doi:10.1002/nsg.12149
Scherler, D. (2014). Climatic limits to headwall retreat in the Khumbu Himalaya, eastern Nepal. *Geology, 42*(11), 1019-1022. doi:10.1130/g35975.1
Scherler, D., Bookhagen, B., & Strecker, M. R. (2011). Hillslope-glacier coupling: The interplay of topography and glacial dynamics in High Asia. *Journal of Geophysical Research: Earth Surface, 116*(F2). doi:10.1029/2010JF001751
Schmid, M. O., Gubler, S., Fiddes, J., & Gruber, S. (2012). Inferring snowpack ripening and melt-out from distributed measurements of near-surface ground temperatures. *The Cryosphere, 6*(5), 1127-1139. doi:10.5194/tc-6-1127-2012
Schrott, L., Hufschmidt, G., Hankammer, M., Hoffmann, T., & Dikau, R. (2003). Spatial distribution of sediment storage types and quantification of valley fill deposits in an

alpine basin, Reintal, Bavarian Alps, Germany. *Geomorphology*, *55*(1–4), 45-63. doi:10.1016/S0169-555X(03)00131-4

Segall, P. (1984). Rate-dependent extensional deformation resulting from crack growth in rock. *Journal of Geophysical Research: Solid Earth*, *89*(B6), 4185-4195. doi:10.1029/JB089iB06p04185

Selby, M. J. (1980). A rock mass strength classification for geomorphic purposes: with tests from Antarctica and New Zealand. *Zeitschrift Fur Geomorphologie*, *24*(1), 31-51.

Shobe, C. M., Hancock, G. S., Eppes, M. C., & Small, E. E. (2017). Field evidence for the influence of weathering on rock erodibility and channel form in bedrock rivers. *Earth Surface Processes and Landforms*, *42*(13), 1997-2012. doi:10.1002/esp.4163

Statham, I. (1976). A scree slope rockfall model. *Earth Surface Processes*, *1*(1), 43-62. doi:10.1002/esp.3290010106

Strunden, J., Ehlers, T. A., Brehm, D., & Nettesheim, M. (2015). Spatial and temporal variations in rockfall determined from TLS measurements in a deglaciated valley, Switzerland. *Journal of Geophysical Research: Earth Surface*, *120*(7), 1251-1273. doi:10.1002/2014jf003274

Thapa, P., Martin, Y. E., & Johnson, E. A. (2017). Quantification of controls on regional rockfall activity and talus deposition, Kananaskis, Canadian Rockies. *Geomorphology*. doi:10.1016/j.geomorph.2017.09.039

Walder, J., & Hallet, B. (1985). A Theoretical-Model of the Fracture of Rock During Freezing. *Geological Society of America Bulletin*, *96*(3), 336-346. doi:10.1130/0016-7606(1985)96<336:ATMOTF>2.0.CO;2

Walder, J. S., & Hallet, B. (1986). The Physical Basis of Frost Weathering - toward a More Fundamental and Unified Perspective. *Arctic and Alpine Research*, *18*(1), 27-32. doi:10.2307/1551211

Weber, S., Fäh, D., Beutel, J., Faillettaz, J., Gruber, S., & Vieli, A. (2018). Ambient seismic vibrations in steep bedrock permafrost used to infer variations of ice-fill in fractures. *Earth and Planetary Science Letters, 501*, 119-127. doi:10.1016/j.epsl.2018.08.042

Wegmann, M. (1998). *Frostdynamik in hochalpinen Felswänden am Beispiel der Region Jungfraujoch - Aletsch.* (PhD Thesis), Zürich.

Wegmann, M., & Gudmundsson, G. H. (1999). Thermally induced temporal strain variations in rock walls observed at subzero temperatures. In K. Hutter, Y. Wang, & H. Beer (Eds.), *Advances in Cold-Region Thermal Engineering and Sciences* (Vol. 533, pp. 511-518). Berlin, Heidelberg: Springer doi:10.1007/BFb0104208

Wegmann, M., Gudmundsson, G. H., & Haeberli, W. (1998). Permafrost Changes in Rock Walls and the retreat of alpine glaciers: a Thermal Modelling Approach. *Permafrost And Periglacial Processes, 9,* 23-33. doi:10.1002/(SICI)1099-1530(199801/03)9:1<23::AID-PPP274>3.0.CO;2-Y

Wegmann, M., & Keusen, H.-R. (1998). *Recent geophysical investigations at a high alpine permafrost construction site in Switzerland.* Paper presented at the 7th International Conference on Permafrost Yellowknife, Canada.

Whipple, K. X., Kirby, E., & Brocklehurst, S. H. (1999). Geomorphic limits to climate-induced increases in topographic relief. *Nature, 401*(6748), 39-43. doi:10.1038/43375

Wirz, V., Schirmer, M., Gruber, S., & Lehning, M. (2011). Spatio-temporal measurements and analysis of snow depth in a rock face. *The Cryosphere, 5*(4), 893-905. doi:10.5194/tc-5-893-2011

Zhang, Z. X. (2002). An empirical relation between mode I fracture toughness and the tensile strength of rock. *International Journal of Rock Mechanics and Mining Sciences, 39*(3), 401-406. doi:10.1016/S1365-1609(02)00032-1

Tables

Table 1. Altitude, exposition, slope angle, 1^{st} to 3^{rd} quartile and mean of rock strength measured with the Schmidt hammer, 1^{st} to 3^{rd} quartile and mean of fracture spacing and rock mass strength (RMS) of instrumented rockwalls

Rockwall	Altitude (m)	Exposition (°)	Slope (°)	Rock Strength (Q)	Fracture spacing (m)	RMS
				1^{st} – 3^{rd} Qu. (Mean)	1^{st} – 3^{rd} Qu. (Mean)	
RW1-S*	3158	154	79	45 - 58 (53)	1.65 – 2.98 (2.82)	77
RW1-N*	3157	33	90	45 – 48 (46)	0.24 – 1.16 (0.85)	72
RW2	2907	70	78	46 – 52 (49)	0.12 – 0.50 (0.37)	73
RW3-S$^+$	2723	148	71	30 – 34 (31)	0.10 – 0.41 (0.32)	62
RW3-N	2674	311	85	59 – 68 (64)	0.13 – 0.52 (0.43)	74
RW4	2580	17	87	37 - 42 (39)	0.31 – 1.00 (0.67)	70

Table 2. Model parameters

Parameter		Aplite	Amphibolite	Quartz slate
		value (range)	value (range)	value (range)
All models				
Rock density (kg m^{-3})	ρ_s	2760	2970	2800
Assumed (*measured*) rock porosity (%)	n_r	3 (*0.89 ±0.02*)	3 (*0.52 ±0.11*)	3 (*0.80 ±0.17*)
Rock thermal conductivity[a] (W m^{-1} K^{-1})	λ_s	2.8 (1 – 3.8)	1.54 (1.3 – 1.7)	2.5 (1 – 4.1)
Rock specific heat capacity[a] (kJ kg^{-1} K^{-1})	c_s	0.80 (0.67 – 1.05)	0.75 (0.67 – 0.88)	0.80 (0.67 – 1.05)
Rock thermal diffusivity (m² s^{-1})	κ	1.23 (0.33 – 1.99)	0.67 (0.49 – 0.83)	1.08 (0.33 – 2.12)
Latent heat (kJ kg^{-1})	L		334	
Rock water content (%)	W		3	
Water content below pore freezing point[b] (%)	W_u		5	
Ice density (kg m^{-3})	ρ_i		920	
Ice thermal conductivity (W m^{-1} K^{-1})	λ_i		2.24	
Ice specific heat capacity (kJ kg^{-1} K^{-1})	c_i		2.09	
Water density (kg m^{-3})	ρ_w		1000	
Water thermal conductivity (W m^{-1} K^{-1})	λ_w		0.56	
Water specific heat capacity (kJ kg^{-1} K^{-1})	c_w		4.18	
Thermo-mechanical models				
Critical fracture toughness[d] (MPa m$^{1/2}$)	K_C	1.9 (1.6 – 2.1)	2.2 (1.9 -3.1)	1.7 (1.3 – 2.0)
Walder and Hallet (1985)				
Pore freezing point[c] (°C)	T_f		-1	
Hydraulic conductivity[c] (m s^{-1})	k_{hc}		5×10^{-14}	
Grain size[c] (mm)	R		0.75	
Liquid layer thickness[c] (nm °C$^{1/2}$)	h_l		6	
Initial crack radius[c] (m)	x_i		0.05	
Angle between crack plane and rockwall[c] (°)	ϕ		0	
Poisson' ratio ()	ν	0.339	0.3205	0.263
Shear modulus (GPa)	G	16.73	35.34	23.05
Critical fracture toughness[d] (MPa m$^{1/2}$)	K_C	1.87	2.19	1.66
Growth-law parameter[c] (m s^{-1})	V_c	340	340	340
Growth-law parameter[c] ()	γ	37.1	37.1	37.1
Rempel et al. (2016)				
Bulk melting temperature[e] (K)	T_m		273	
Unfrozen permeability[f] (m²)	k_{p0}		10^{-18} (10^{-18} – 10^{-14})	
Power law exponent[e] ()	α		4	
Undercooling for ice formation[e] (°C):	ΔT_f		0.1	

[a]*Cermák and Rybach* [1982], [b]*Anderson et al*. [2013], [c]*Walder and Hallet* [1985] with values from *Atkinson and Rawlings* [1981], *Gilpin* [1979, 1980] and [*Segall*, 1984] [d]*Draebing and Krautblatter* [2019], [e]*Rempel et al.* [2016] with values from *Andersland and Ladanyi* [2004], [f]*Krautblatter* [2009]

Table 3. Mean annual air temperature (MAAT), mean annual rock surface temperature (MARST), snow duration, mean winter air temperature (MWAT), mean winter rock surface temperature (MWRST), mean summer air temperature (MSAT) and mean summer rock surface temperature (MSRST) values for meteorological station and temperature loggers.

	MAAT/MARST (°C)			snow duration (d)			MWAT/MWRST (°C)			MSAT/MSRST (°C)		
Logger	2016/17	2017/18	2018/19	2016/17	2017/18	2018/19	2016/17	2017/18	2018/19	2016/17	2017/18	2018/19
Meteo Station	-0.6	-1.0	-1.1	216	225	246	-6.5	-9.1	-7.1	6.6	5.9	6.8
RW1-S*	NA	0.3	1.4	NA	150	138	NA	-7.3	-6.9	NA	9.3	10.1
RW1-N*	NA	-1.9	-1.1	NA	161	120	NA	-8.8	-8.5	NA	7.4	8.0
RW2	-1.7	-1.7	-1.4	207	224	245	-7.5	-6.3	-5.3	5.9	4.2	4.3
RW3-S^{+}	NA	5.6	7.8	NA	81	5	NA	-4.1	-0.7	NA	15.9	16.2
RW3-N	0.9	1.0	1.8	228	227	233	-3.6	-2.3	-1.2	8.6	7.3	7.7
RW4	0.7	1.5	1.8	220	220	223	-4.4	-1.8	-1.6	7.6	7.3	7.4

* 29 Aug 2017 - 28 Aug 2019, $^{+}$ 2017/18 – 2018/19

Table 4. Maximum modelled frost cracking intensity (FCI), depth of maximum FCI, depth range of frost cracking for HR-, A-, WH- and R-model.

Rockwall	Maximum frost cracking intensity				Depth of maximum FCI (m)				Depth range of frost cracking (m)			
	HR (°C-day/dm)	A (°C-day/dm)	WH (m)	R (%)	HR	A	WH	R	HR	A	WH	R
RW1-S	1.17 - 1.32	0.21 - 0.32	0.27 - 0.38	0.07	0.1 - 0.3	0.1 – 0.3	0.8 - 0.9	0.1	0.1 - 1.8	0.1 - 1.8	0.1 - 1.8	0.1 - 1.0
RW1-N	0.06 - 0.14	0.03 - 0.04	0.16 - 0.17	0.02 - 0.03	0.1	0.1	0.3 - 1.1	0.1 - 0.9	0.1 - 0.2	0.1 - 0.2	0.1 - 3.1	0.1 - 1.7
RW2	0 - 0.08	0 - 0.01	0.11 - 0.13	0.01 - 0.02	0.1	0.1	0.2 - 0.5	0.1 - 0.3	0 - 0.4	0 - 0.4	0.1 - 2.0	0.1 - 1.3
RW3-S	1.53 - 1.71	0.39 - 0.64	0.11 - 0.19	0.10 - 0.15	0.1	0.1	0.1 - 0.3	0.1	0.1 - 0.9	0.1 - 0.9	0.1 - 1.0	0.1 - 0.5
RW3-N	0 - 0.68	0 - 0.08	0.10 - 0.11	0	0.1	0.1	0.1	NF	0.1 - 0.7	0 - 0.7	0.1 - 0.4	0
RW4	0.07 - 0.67	0.01 - 0.04	0.10 - 0.19	0 - 0.01	0.1	0.1	0.1	0.1	0 - 1.1	0.1 - 1.1	0.1 - 1.0	0 - 0.2

Figure Captions

Figure 1. a The research area is located in the Swiss Alps (inset map). Hillshade map showing locations of instrumented rockwalls (Swiss Alti3D 2 m DEM provided by the Federal Office of Topography, swisstopo). Overview photos of the **b** Hungerli valley and **c** the Steintaelli ridge.

Figure 2. Schematic illustration of **a** the research set up, **b** the model approach and **c** the results and validation approach.

Figure 3. a Meteorological station data from Oberer Stelligletscher at 2910 m and **b-g** temperature logger data plotted from 1 September 2016 to 31 August 2019. **a** Light grey rectangles highlight the interpolated air temperature, while **b-g** light grey rectangles highlight the snow cover period and dark grey rectangles the zero-curtain period.

Figure 4. Modelled frost cracking in terms of frost cracking intensity, crack length or porosity change for **a-d** RW1-S, **e-h** RW1-N, **i-l** RW2, **m-p** RW3-S, **q-t** RW3-N and **u-x** RW4 using the models by *Hales & Roering* [2007], *Anderson et al.* [2013], *Walder & Hallet* [1985] and *Rempel et al.* [2016] plotted versus rock depth.

Figure 5. Sensitivity analysis of rock thermal diffusivity for the models by **a** *Hales & Roering* [2007], **b** *Anderson et al.* [2013], **c** *Walder & Hallet* [1985] and **d** *Rempel et al.* [2016]. Sensitivity analysis of **e** hydraulic conductivity and **f** hydraulic permeability, **g-h** initial crack length and **i-j** fracture toughness of the models by *Walder & Hallet* [1985] and *Rempel et al.* [2016]. Modelled results of logger RW1-N from 2018/19 and RW4 from 2016/17 are exemplary shown, for a complete sensitivity analysis see Figures S2 to S5 in the supporting information.

Figure 6. Modelled mean cracking intensity of **a** *Hales & Roering* [2007] and **b** *Anderson et al.* [2013], **c** modelled crack length using the model by *Walder & Hallet* [1985], **d** modelled depth-integrated porosity change using the model by *Rempel et al.* [2016] plotted versus altitude. The error bars present the minimum and maximum modelled frost cracking of each model. **e** Boxplots of measured rock strength and **f** fracture spacing plotted for each rockwall. Diamonds present mean values of rock strength and fracture spacing.

Figure 1.

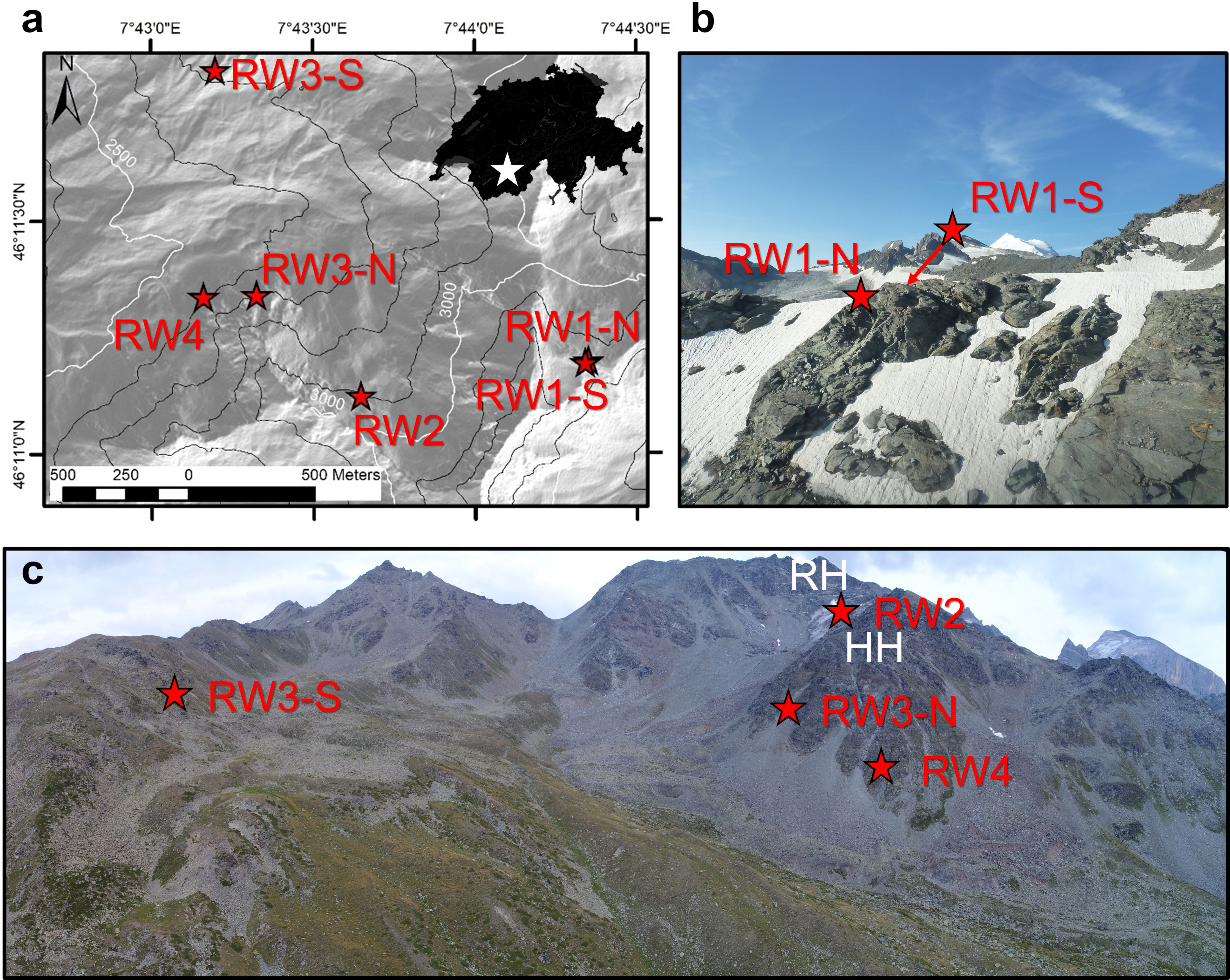
a
7°43'0"E
7°43'30"E
7°44'0"E
7°44'30"E
46°11'30"N
46°11'0"N
N
RW3-S
2500
RW3-N
RW4
3000
RW1-N
RW1-S
RW2
3000
500
250
0
500 Meters
b
RW1-S
RW1-N
c
RH
RW2
HH
RW3-S
RW3-N
RW4

Figure 2.

a
Set Up
North
South
Altitude (m)
3200
3100
3000
2900
2800
2700
2600
2500
Permafrost
Temperature Logger
b
Model approach
0
10 m
Snow
Hales and Roering
Anderson et al.
Walder and Hallet
Ice lenses
Rempel et al.
0 m
10 m
c
Results and validation
frost cracking peak
0
10
Depth (m)
depth of peak
lower limit
Frost Cracking
Q
Fracture Density

Figure 3.

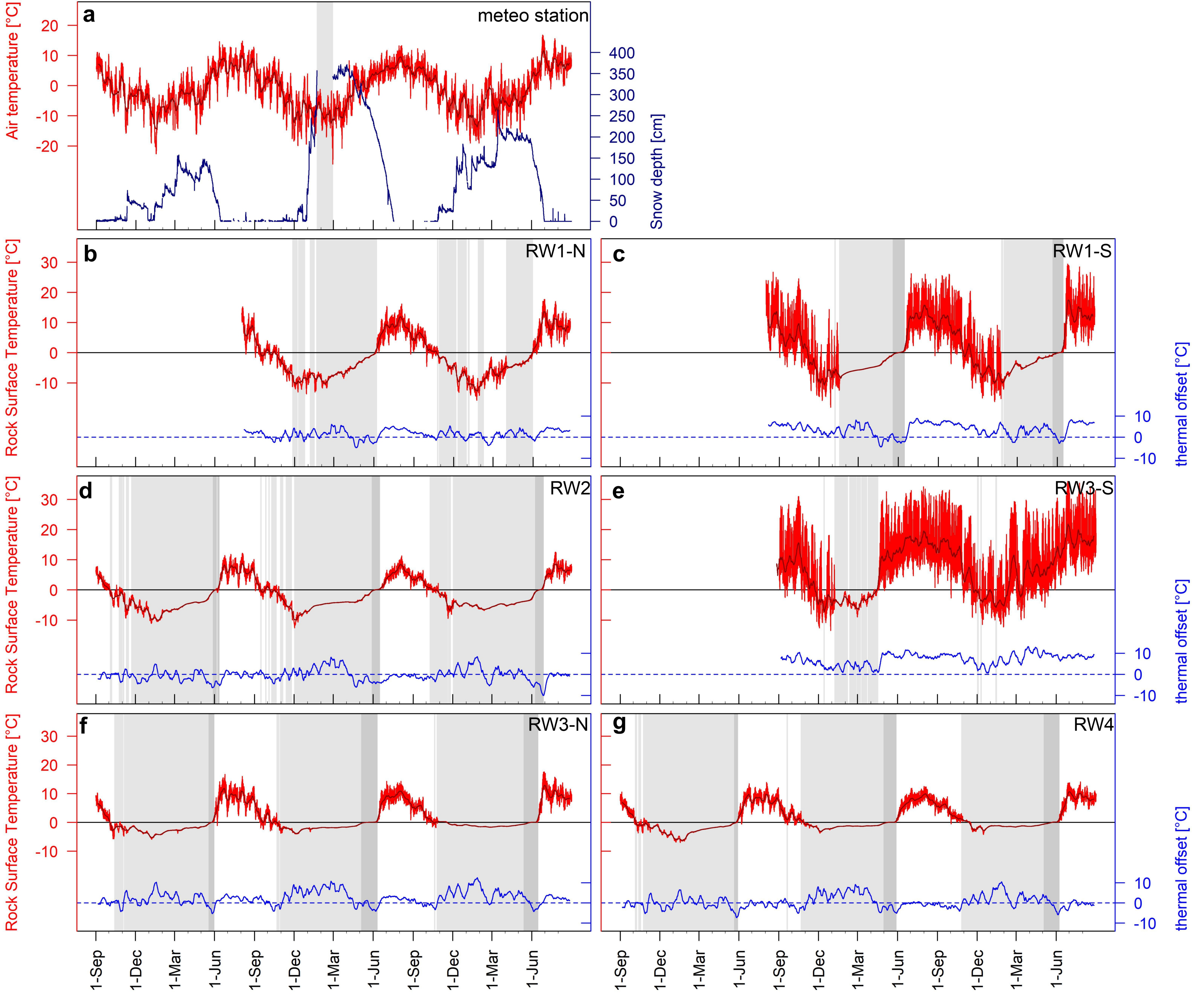

a
meteo station
Air temperature [°C]
Snow depth [cm]
b
RW1-N
c
RW1-S
d
RW2
e
RW3-S
f
RW3-N
g
RW4
Rock Surface Temperature [°C]
thermal offset [°C]
1-Sep
1-Dec
1-Mar
1-Jun

Figure 4.

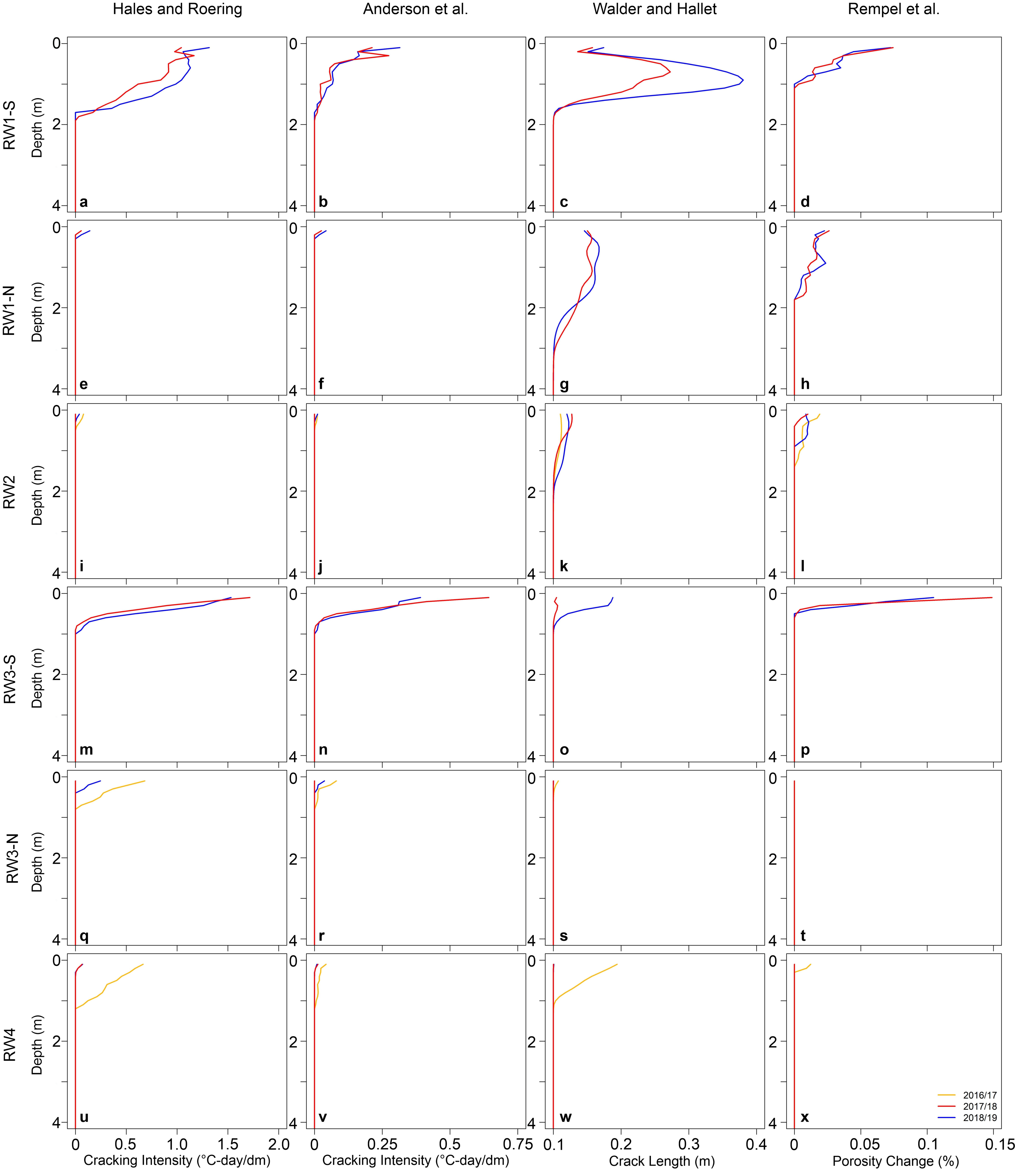

Hales and Roering
Anderson et al.
Walder and Hallet
Rempel et al.
RW1-S
RW1-N
RW2
RW3-S
RW3-N
RW4
Depth (m)
a
b
c
d
e
f
g
h
i
j
k
l
m
n
o
p
q
r
s
t
u
v
w
x
2016/17
2017/18
2018/19
Cracking Intensity (°C-day/dm)
Cracking Intensity (°C-day/dm)
Crack Length (m)
Porosity Change (%)

Figure 5.

Hales and Roering
Anderson et al.
Rock Thermal Diffusivity
Depth (m)
Cracking Intensity (°C-day/dm)
a
b
Walder and Hallet
Rempel et al.
Crack Length (m)
Porosity Change (%)
c
d
1.08 m² s⁻¹
0.33 m² s⁻¹
2.12 m² s⁻¹
RW1-N (2018/19)
RW4 (2016/17)
Walder and Hallet
Rempel et al.
Hydraulic Properties
e
f
min
max
RW1-N (2018/19)
RW4 (2016/17)
Initial Crack Length
g
h
10 cm
1 cm
RW1-N (2018/19)
RW4 (2016/17)
Fracture Toughness
i
j
1.7 MPa m^1/2
1.3 MPa m^1/2
2.0 MPa m^1/2
RW1-N (2018/19)
RW4 (2016/17)

Figure 6.

Hales and Roering
Anderson et al.
Walder and Hallet
Rempel et al.
Rock Strength
Fracture Spacing
Altitude (m)
3200
3100
3000
2900
2800
2700
2600
2500
RW1-S
RW3-N = 0
QS
AP
AM
a
b
c
d
e
f
RW1-S
RW1-N
RW2
RW3-S
RW3-N
RW4
Cracking Intensity (°C-day/dm)
Cracking Intensity (°C-day/dm)
Crack Length per Depth (m/m)
Λ (mm)
Q
Spacing (m)